Peri-Siberian Ordovician to Devonian tectonic switching in the Olkhon Terrane (southern Siberia): Structural and geochronological constraints

Zhi-yong Li, Ying-de Jiang, Stephen Collett, Pavla Štípská, Karel Schulmann, Sheng Wang, Vasiliy Sukhorukov, Xiu-juan Bai, Wan-feng Zhang

To cite this version:

Zhi-yong Li, Ying-de Jiang, Stephen Collett, Pavla Štípská, Karel Schulmann, et al.. Peri-Siberian Ordovician to Devonian tectonic switching in the Olkhon Terrane (southern Siberia): Structural and geochronological constraints. Tectonics, 2023, 10.1029/2023TC007826 . hal-04222094

HAL Id: hal-04222094
https://hal.science/hal-04222094

Submitted on 12 Feb 2024

Tectonics®

RESEARCH ARTICLE
10.1029/2023TC007826

Key Points:

- The Olkhon Terrane underwent Cambrian–Silurian shortening-extension cycles and Devonian lateral extrusion and shearing
- Cambrian to Devonian tectonic switches in the Olkhon Terrane mark the collisional evolution of peri-Siberian orogenic system
- Geodynamic evolution of the Olkhon Terrane closely matches to that of central segment of the Mongolian Collage

Supporting Information:

Supporting Information may be found in the online version of this article.

Correspondence to:

Y.-D. Jiang,
jiangyd@gig.ac.cn

Citation:

Li, Z.-Y., Jiang, Y.-D., Collett, S., Štípská, P., Schulmann, K., Wang, S., et al. (2023). Peri-Siberian Ordovician to Devonian tectonic switching in the Olkhon Terrane (southern Siberia): Structural and geochronological constraints. *Tectonics*, *42*, e2023TC007826. https://doi.org/10.1029/2023TC007826

Received 2 MAR 2023
Accepted 10 SEP 2023

Peri-Siberian Ordovician to Devonian Tectonic Switching in the Olkhon Terrane (Southern Siberia): Structural and Geochronological Constraints

Zhi-Yong Li[1,2,3,4], Ying-De Jiang[1,3], Stephen Collett[2], Pavla Štípská[2], Karel Schulmann[2,5], Sheng Wang[6], Vasiliy Sukhorukov[7], Xiu-Juan Bai[8], and Wan-Feng Zhang[1,3,4]

[1]State Key Laboratory of Isotope Geochemistry, Guangzhou Institute of Geochemistry, Chinese Academy of Sciences, Guangzhou, China, [2]Centre for Lithospheric Research, Czech Geological Survey, Prague, Czech Republic, [3]CAS Center for Excellence in Deep Earth Science, Guangzhou, China, [4]University of Chinese Academy of Sciences, Beijing, China, [5]Université de Strasbourg, CNRS, ITES, UMR 7063, Strasbourg, France, [6]School of Civil Engineering, Anhui Jianzhu University, Hefei, China, [7]V.S. Sobolev Institute of Geology and Mineralogy SB RAS, Novosibirsk, Russia, [8]Key Laboratory of Tectonics and Petroleum Resources, Ministry of Education, China University of Geosciences, Wuhan, China

Abstract The Olkhon Terrane is thought to preserve a record of the initial collision of the Siberian Craton with its peripheral orogenic system during the early Paleozoic. However, the related tectono-metamorphic process and its time-scale remain obscure. To address this issue, new structural observations combined with U-Pb zircon and monazite and $^{40}Ar/^{39}Ar$ biotite geochronology were conducted in the migmatitic-granitic Anga-Sakhurta Zone of the terrane. An earliest syn-collisional event associated with the development of a c. 500–480 Ma sub-horizontal migmatitic fabric is confirmed. This early fabric was affected by later extensional doming in association with emplacement of partial melts (in terms of c. 470–445 Ma granite sills) parallel to the sub-horizontal mechanical anisotropy. Subsequent upright folding leading to amplification of extensional domal structures and heterogeneous vertical transposition of composite horizontal fabric occurred soon after the doming, as indicated by intrusions of residual melts into the axial planes of the upright folds. The latest episode of deformation was marked by development of greenschist-facies sinistral shear zones surrounding the Anga-Sakhurta Zone at c. 420–400 Ma. An updated tectonic model involving (a) Middle–Late Ordovician crustal thinning associated with horizontal crustal flow, (b) Silurian crustal shortening related to northwards movement of Cambrian magmatic arc of the Birkhin Complex to the south, and (c) Early Devonian lateral extrusion and sinistral shearing associated with progression of the Birkhin Complex promontory, is proposed. Results from this study shed lights on the collisional evolution of peri-Siberian orogenic system during the early stage evolution of the Central Asian Orogenic Belt.

1. Introduction

The Phanerozoic Central Asian Orogenic Belt (CAOB) recorded massive continental growth of more than 5.3 million square kilometers, via lateral amalgamation of diverse lithological units and vertical addition of juvenile mantle components (Sengor et al., 1993; Wilde, 2015; Windley et al., 2007). There is a consensus that the accretionary evolution of the CAOB developed by peripheral additions of oceanic and continental fragments to the Siberian Craton margin from the late Proterozoic to early Paleozoic times (Cocks & Torsvik, 2007; Zonenshain et al., 1990). The Sayan-Baikal collisional belt (Donskaya et al., 2000), located at the southern margin of the Siberian Craton (Figure 1, inset) (Gladkochub et al., 2008b), is an early Paleozoic collisional system forming the northern branch of the Mongolian Collage of the CAOB (Delvaux et al., 1995). This system consists of Proterozoic ophiolitic units interpreted as arc and back-arc assemblages, metamorphosed Precambrian para- and ortho-gneiss and granitoids of Cambrian to Silurian age (e.g., Gordienko et al., 2007; Makrygina et al., 2007; Zorin et al., 2009). These features together with preservation of significant early Paleozoic high-grade metamorphism and deformation led these authors to consider the Sayan-Baikal collisional belt to represent the earliest and most important collisional peri-Siberian orogenic system.

The Olkhon Terrane is the best exposed zone of the Sayan-Baikal collisional belt and therefore represents a pivotal area for understanding the tectono-metamorphic evolution related to the earliest stages of CAOB formation. Lithological, metamorphic and geochronological differences led several authors to divide the Olkhon Terrane into tectonic zones that are generally sub-parallel to the Siberian margin (e.g., Fedorovsky & Sklyarov, 2015). From

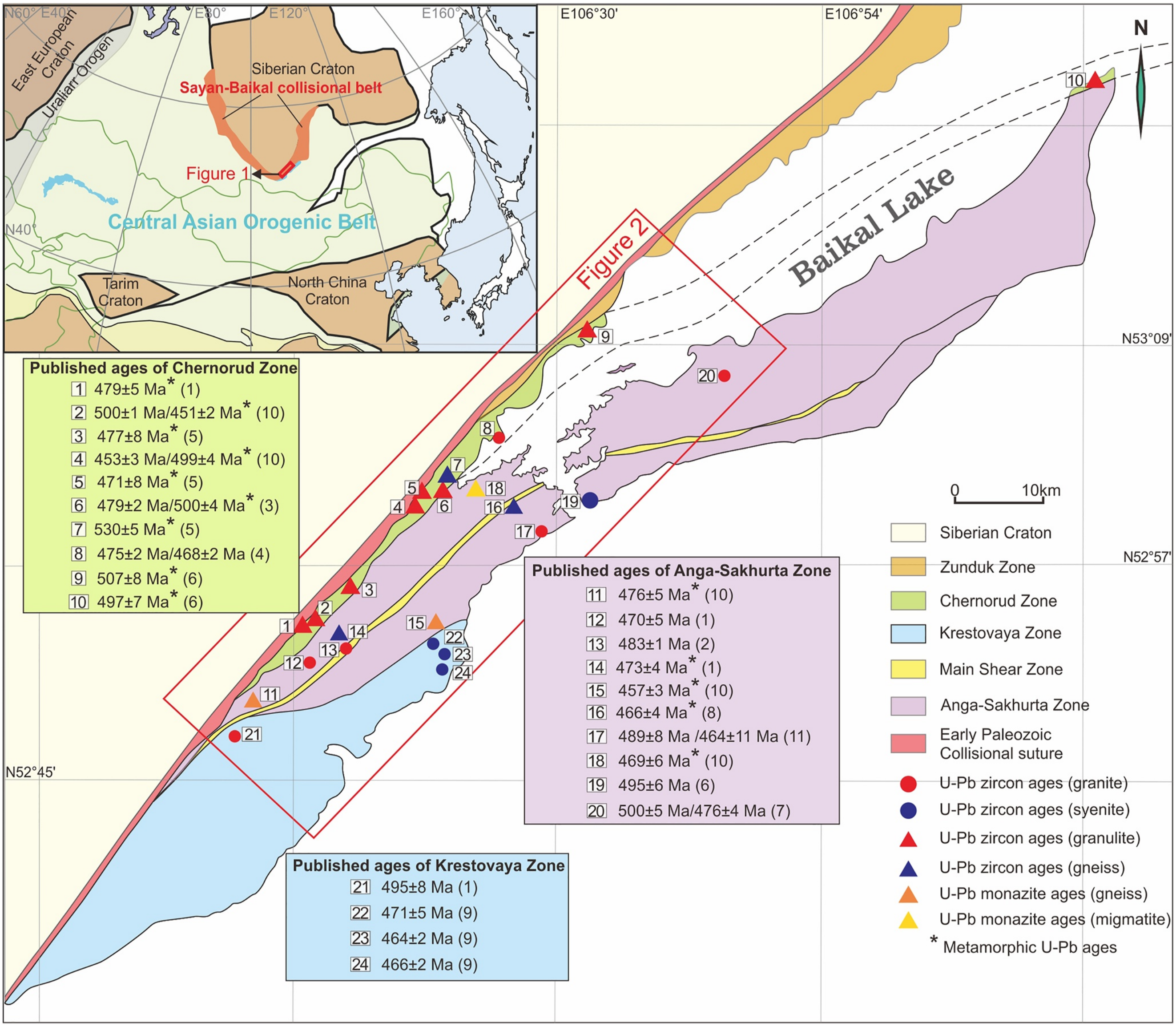

Published ages of Chernorud Zone	
1	479±5 Ma* (1)
2	500±1 Ma/451±2 Ma* (10)
3	477±8 Ma* (5)
4	453±3 Ma/499±4 Ma* (10)
5	471±8 Ma* (5)
6	479±2 Ma/500±4 Ma* (3)
7	530±5 Ma* (5)
8	475±2 Ma/468±2 Ma (4)
9	507±8 Ma* (6)
10	497±7 Ma* (6)

Published ages of Anga-Sakhurta Zone	
11	476±5 Ma* (10)
12	470±5 Ma (1)
13	483±1 Ma (2)
14	473±4 Ma* (1)
15	457±3 Ma* (10)
16	466±4 Ma* (8)
17	489±8 Ma /464±11 Ma (11)
18	469±6 Ma* (10)
19	495±6 Ma (6)
20	500±5 Ma/476±4 Ma (7)

Published ages of Krestovaya Zone	
21	495±8 Ma (1)
22	471±5 Ma (9)
23	464±2 Ma (9)
24	466±2 Ma (9)

Figure 1. Simplified tectonic map of the Olkhon Terrane, modified after Donskaya et al. (2017). Inset shows position of the Sayan-Baikal collisional belt with respect to the Central Asian Orogenic Belt (Modified after Shu et al. (2022)). Available zircon/monazite U-Pb ages for metamorphic and igneous rocks are indicated, with data sourced from: (1) Donskaya et al. (2017); (2) Mikheev et al. (2017); (3) X. C. Li et al. (2009); (4) Mekhonoshin et al. (2013); (5) Vladimirov et al. (2011); (6) Gladkochub et al. (2008b); (7) Makrygina et al. (2014); (8) Sklyarov et al. (2020b); (9) Sklyarov et al. (2009); (10) Z. Y. Li et al. (2023); and (11) Donskaya et al. (2013).

north to south these are the Zunduk, Chernorud, Anga-Sakhurta, and Krestovaya zones (Figure 1) that are separated from each other by mylonitic shear zones and differ in terms of metamorphic grade, structure and relative abundance of metamorphic and igneous rocks (Donskaya et al., 2017). Recent advances in geochronology and geochemistry allowed the definition of individual zones as late Proterozoic and early Paleozoic arcs, early Paleozoic back-arc and Precambrian continental fragments, respectively, all of which were considered to accrete to the Siberian Craton from the Cambrian to the Ordovician (Donskaya et al., 2017; Fedorovsky & Sklyarov, 2015; Gladkochub et al., 2008b).

Fedorovsky (1997) and Fedorovsky and Sklyarov (2015) proposed that the tectonic evolution of the Olkhon Terrane started with an early nappe stacking leading to the development of recumbent folds and sub-horizontal high-temperature (HT) fabrics associated with collision of the Olkhon Terrane with the Siberian Craton. It is generally accepted that this event occurred at around 500–490 Ma based on U-Pb ages of granulite facies rocks and syntectonic granite, primarily in the Chernorud Zone (Figure 1) (Donskaya et al., 2013; Gladkochub et al., 2008b; Vladimirov et al., 2011). This event was followed by the development of vertical sinistral shear zones, which surrounded low strain domains in the central Anga-Sakhurta Zone. These low strain domains are characterized by wide regions containing migmatite-granite gneiss domes mantled by medium grade quartzite, marble, and amphibolite. The tectonic significance of anatexis and emplacement of syntectonic granitoids and numerous dykes are considered to be linked to the doming process that was allegedly governed by the early stages of sinistral wrenching (Fedorovsky et al., 2010; Mikheev et al., 2017). The timing of this HT event was constrained by a second generation of 470–460 Ma syn-tectonic granitoids, primarily in the Anga-Sakhurta Zone (Fedorovsky et al., 2005; Makrygina et al., 2014; Sklyarov et al., 2009).

The southernmost Krestovaya Zone is essentially formed by the c. 500 Ma Birkhin Complex (Gladkochub et al., 2014), which is interpreted as a magmatic arc (Donskaya et al., 2017). It is proposed that the Birkin Complex formed a rigid indenter responsible for lateral extrusion of the Anga-Sakhurta Zone, which was accommodated by sinistral shear zones (e.g., Fedorovsky & Sklyarov, 2015). Fedorovsky (1997) and many others later considered this structural pattern to be a key element of the central part of the Olkhon Terrane. Existing regional ^{40}Ar/^{39}Ar geochronological data defined two groups of ages at c. 440–435 (muscovite and amphibole) and c. 415–410 Ma (muscovite and biotite), which were interpreted to reflect post-amphibolite facies cooling and late-orogenic shearing, respectively (Travin et al., 2009; Vladimirov et al., 2011; Volkova et al., 2008). Such a distribution of ^{40}Ar/^{39}Ar ages may challenge the generally accepted notion that the sinistral shearing was temporally connected to the main HT event. Accordingly, the timing and formation of the migmatite-magmatite domes under the context of the tectono-thermal history of the central Anga-Sakhurta Zone remain enigmatic. The other challenge is the alleged causal and temporal relationship between growth of domes and sinistral strike-slip movements, which remains unconstrained.

To contribute to these issues, a detailed structural and geochronological (U-Pb zircon and monazite) study of migmatite and granite veins located in the central Anga-Sakhurta Zone of the Olkhon Terrane were carried out. In addition, ^{40}Ar/^{39}Ar geochronology study of the Chernorud, Anga-Sakhurta and Krestovaya zones and their surrounding shear zones was performed, aiming to better constrain the activity of crustal scale wrench zones and cooling of the whole system. These data allow not only to precise the timing of tectonic events advocated by previous researchers but also to propose an updated scenario for the early stages of peri-Siberian collision exemplified by the geodynamic evolution of the Olkhon Terrane.

2. Geological Setting

The Olkhon Terrane is separated from the Siberian Craton by the Cenozoic Primorsky Fault that was related to the opening of the Baikal Lake rift (Figure 1) (Fedorovsky & Sklyarov, 2015). This terrane is composed of sedimentary, volcanic and plutonic rocks that were metamorphosed at amphibolite to granulite facies conditions, with the degree of metamorphism generally increasing from southeast to northwest (Donskaya et al., 2017; Gladkochub et al., 2010, 2013). According to lithological differences, degree of metamorphism, characters of igneous rocks and prevailing structure, the Olkhon Terrane has been divided into four regional-scale NE-striking tectonic zones: the granulite facies Zunduk and Chernorud Zones in the north, the upper amphibolite facies Anga-Sakhurta Zone in the center and the lower amphibolite facies Krestovaya Zone in the south (Figure 1).

The Zunduk Zone is composed primarily of late Neoproterozoic gneissic granite and paragneiss typical of the whole Olkhon Terrane as well as two exotic tectonic slices of late Paleoproterozoic (Kaltygey Complex) and early Neoproterozoic (Ust-Zunduk Complex) ages. Metapelitic granulite of the Kaltygey Complex contains Paleoproterozoic and Archean detrital zircons with metamorphic rims dated at c. 1,870 Ma (Volkova et al., 2021). A similar age (1,873 ± 6 Ma) is recorded in zircon cores from a gneissic granite that has a whole-rock $\varepsilon_{\mathrm{Nd}}(t)$ value of -1.1 (Donskaya et al., 2017). Notably, there are no chemical or isotopic equivalents to these rocks in the adjacent Siberian Craton (Donskaya et al., 2017; Poller et al., 2005). The Ust-Zunduk Complex consists of foliated orthogneiss with a U-Pb zircon age of 807 ± 9 Ma and a whole-rock $\varepsilon_{\mathrm{Nd}}(t)$ value of -5.5 (Donskaya et al., 2017). Metamorphism in the Zunduk Zone reaches granulite facies, exemplified by development of garnet-orthopyroxene-cordierite, orthopyroxene-cordierite, and garnet-cordierite-biotite assemblages (Donskaya et al., 2017). Volkova et al. (2021) estimated peak conditions of a Kaltygey Complex metapelitic granulite at around 950ºC and 9 kbar, and, together with their old metamorphic zircon ages, these authors proposed a late Paleoproterozoic HT metamorphic event in the region. Nonetheless, these authors also identified subsequent reworking in the early Paleozoic as evidenced by c. 540 and c. 480 Ma ^{40}Ar/^{39}Ar ages of amphibole and biotite from the same samples.

The Chernorud Zone is characterized by mafic garnet- clinopyroxene-amphibole bearing granulite and intermediate to felsic granulite mainly consisting of garnet, clinopyroxene, orthopyroxene, plagioclase, K-feldspar, and quartz (Z. Y. Li et al., 2023). Apart from the mafic and felsic granulite, the Chernorud Zone contains numerous highly elongated layers of marble and quartzite that are together with felsic granulite wrapped around mafic and ultra-mafic lenses and boudins (Fedorovsky & Sklyarov, 2015). The protoliths of mafic granulite and orthogneiss of the Chernorud Zone have U-Pb zircon ages 637 ± 4 and 624 ± 11 Ma, respectively (Donskaya et al., 2017; Volkova et al., 2010). Geochemistry of these rocks together with positive whole-rock $\varepsilon_{\mathrm{Nd}}(t)$ values ($\varepsilon_{\mathrm{Nd}}(t) = +6.9$) of orthogneiss indicate that their protolith compositionally corresponds to subduction-related arc type volcanics (Donskaya et al., 2017; Volkova et al., 2010). The protolith of an intermediate garnet two pyroxene granulite was constrained at c. 545 Ma, and its whole-rock $\varepsilon_{\mathrm{Nd}}(t)$ values ranging from +1.8 to +2.1 indicate that it was derived from an enriched mantle source. Chemically, these rocks show OIB geochemical affinities and may represent a fragment of an oceanic guyot (Donskaya et al., 2017). Metamorphic petrology studies revealed peak pressure conditions of 7–11 kbar at 770°–877°C for the granulite facies metamorphism and retrograde amphibolite facies metamorphism at 6.5–6.6 kbar and 695°–732°C (Gladkochub et al., 2008b; X. C. Li et al., 2009; Sklyarov et al., 2020a). Previous studies assumed a Cambrian to Ordovician (c. 510–470 Ma) age for the granulite facies metamorphism (Donskaya et al., 2017; Volkova et al., 2010). In a recent zircon U-Pb geochronological study, Z. Y. Li et al. (2023) inferred two discrete age groups from the granulite at c. 530–500 and c. 450 Ma to represent the timing of granulite and amphioblite facies metamorphism, respectively.

The Anga-Sakhurta Zone occurs in the central part of the Olkhon Terrane and is mainly formed by garnet-sillimanite paragneiss and sillimanite bearing migmatite. Detrital zircons from paragneiss yielded U-Pb ages clustered between c. 530 and 1,000 Ma (Donskaya et al., 2017; Gladkochub et al., 2008b; Volkova et al., 2010). Whole-rock $\varepsilon_{\mathrm{Nd}}(t)$ values for the paragneiss vary from −3.2 to −9.6, and their corresponding T_{DM} model ages are 1.5–2.1 Ga (Donskaya et al., 2017; Gladkochub et al., 2008b; Makrygina et al., 2014). The geochemical compositions of these rocks are comparable with immature greywackes deposited in a back-arc basin setting (Gladkochub et al., 2017). Granitic gneiss in this zone are characterized by LREE enrichment and negative Eu anomalies and are often interpreted as syntectonic leucogranite dykes that intruded the Anga-Sakhurta Zone at c. 470–458 Ma and were gneissified parallel to host rock fabric (Vladimirov et al., 2011). The P_{max} metamorphic conditions of the paragneiss were estimated to 6–8 kbar at 630°–710°C and T_{max} conditions of 770°–790°C at 7.2–7.4 kbar and the retrograde metamorphism corresponds to ~4 kbar and ~670°C (X. C. Li et al., 2009; Makrygina & Petrova, 1998). However, Sklyarov et al. (2020a, 2020b) reported significantly lower metamorphic peak P–T conditions of approximately 4.4–4.8 kbar at 620°–650°C for similar rocks of the region. The timing of this metamorphic evolution was deduced from monazite U-Pb ages, which yielded c. 500 Ma for the P_{max} conditions and c. 450 Ma for the later re-equilibration phase (Z. Y. Li et al., 2023).

The Krestovaya Zone was affected by lower-grade amphibolite facies metamorphism (Donskaya et al., 2017). In the west, it consists of the mafic-dominated Birkhin Complex composed of metamorphosed and gneissified gabbro, pyroxenite, and mafic volcanics, with subordinate felsic subvolcanic rocks and granite. The felsic subvolcanic rocks, granite and gabbro revealed U-Pb zircon ages of c. 500 Ma (Donskaya et al., 2017; Fedorovsky et al., 2005; Yudin et al., 2005). The metamorphosed gabbro and mafic volcanics share similar chemistry of island arc basalt affinity (Donskaya et al., 2017; Fedorovsky et al., 2005; Gladkochub et al., 2014), while the gneissic felsic sub-volcanic rocks and granite are supposedly of subduction related I-type granite affinity (Donskaya et al., 2017). Both mafic and felsic varieties showed positive whole-rock $\varepsilon_{\mathrm{Nd}}(t)$ values of +2.6–+8.1 (Donskaya et al., 2017; Gladkochub et al., 2014; Makrygina et al., 2014). In the east, a narrow strip of the Orso Complex separates the Krestovaya Zone from the Anga-Sakhurta Zone (Figure 2a). This unit is formed by garnet mica-schist, and garnet-biotite fine-grained gneiss containing amphibolite lenses. Gneiss and amphibolite showed compositions corresponding to felsic volcaniclastic and subduction related basalts, respectively (Donskaya et al., 2017; Gladkochub et al., 2010a). Garnet two mica gneiss have whole-rock $\varepsilon_{\mathrm{Nd}}(t)$ values from −2.7 to −7.4 and $T_{\mathrm{DM}} = 1.7$–1.9 Ga (Gladkochub et al., 2010b). Their U-Pb zircon ages fall into two distinct clusters of 792 ± 10 and 844 ± 6 Ma, respectively (Gladkochub et al., 2010a). Metamorphic P–T conditions of metasedimentary rocks of the Orso Complex were estimated at a wide interval of 545°–665°C and 4.4–7.3 kbar (Sklyarov et al., 2020a).

3. Principal Tectono-Metamorphic Features of the Olkhon Terrane

The tectonic models of the Olkhon Terrane are based on excellent quality of geological maps, detailed analyses of satellite and airborne images and structural data summarized by Fedorovsky and Sklyarov (2015). To clarify the tectono-metamorphic features of the region, we use a notation after Beltrando et al. (2008) and Jeřábek

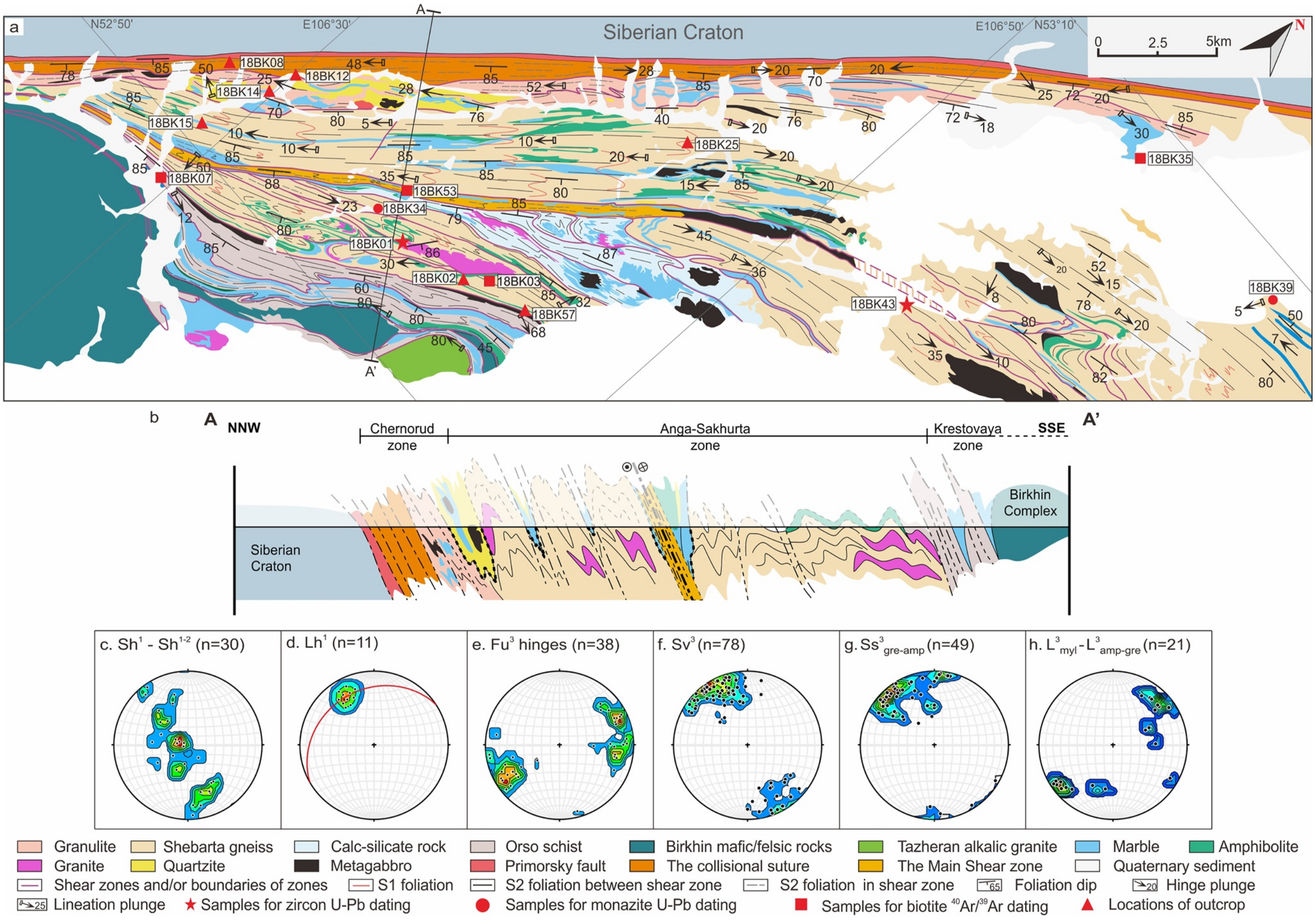

Figure 2. (a) Structural map of the Olkhon Terrane (modified after Fedorovsky et al. (2020) and Fedorovsky and Sklyarov (2015)). (b) Idealized cross-section across the studied region, showing the principal structural features. Sh^1 and Sh^{1-2} represented by solid line, Sv^3 and $Ss^3_{amp\text{-}gre}$ by dot-dashed line, thicker dotted line represents boundary between the orogenic super- and infra-structure. (c–i) Structural diagrams depicting orientation of major structural elements of individual deformation events (equal area lower hemisphere stereographic projection). Structural measurements are from this study except for Lh^1 that are retrieved from Dobrzhinetskaya et al. (1992).

et al. (2012) which reflects the deformation sequences and metamorphic grade in the following way: horizontal foliation, first generation, migmatitic—Sh^1_{MIG}; horizontal foliation, first generation, granulitic—Sh^1_{GRA}; recumbent folds, first generation, migmatite—Fr^1_{MIG}; extensional fabric horizontal, second generation, migmatite Eh^2_{MIG}; foliation horizontal, first and second generation—composite, migmatite—$Sh^{1\text{-}2}_{MIG}$; granite fabric, second generation—S^2_G; upright folds, third generation Fu^3; sinistral shear zone, third generation, amphibolite- to greenschist-facies—$Ss^3_{amp\text{-}gre}$; foliation vertical, third generation—Sv^3.

The structural pattern is different in each of the main tectonic zones that are separated by crustal scale vertical deformation D3 zones associated with the presence of mafic and ultramafic rocks (Figure 2b). The northern Chernorud Zone is characterized by original horizontal granulite facies fabric Sh^1_{GRA} defined by compositional layering in dominant intermediate and felsic granulite, quartzite, mixture of marble and dismembered mafic granulite called "marble mélange" by Russian authors (e.g., Fedorovsky & Sklyarov, 2015) and sheets of syn-tectonic granite. In places the Sh^1_{GRA} is gently to moderately dipping (Figure 2c), this deformation is associated with recumbent (often verticalized by later deformation), isoclinal and sometimes rootless Fr^1_{GRA} folds (e.g., Fedorovsky et al., 2020). These fold hinges and sub-parallel stretching lineations Lh^1 were measured in sites with generally NW-SE trending plunges (Figure 2d) (Dobrzhinetskaya et al., 1992). These up to a hundred meter wide layers are folded by meter to hundred meter-scale upright Fu^3 folds with sub-horizontal hinges (Figures 2e and 3a). One of the characteristic features of the Chernorud Zone is the meter to kilometer scale boudinage of mafic and ultramafic rocks that are scattered parallel to the trend of the main granulite facies foliation that has generally steep attitude. Locally, the granulite show extreme ductile deformation which is transposed to vertical Sv^3 fabric

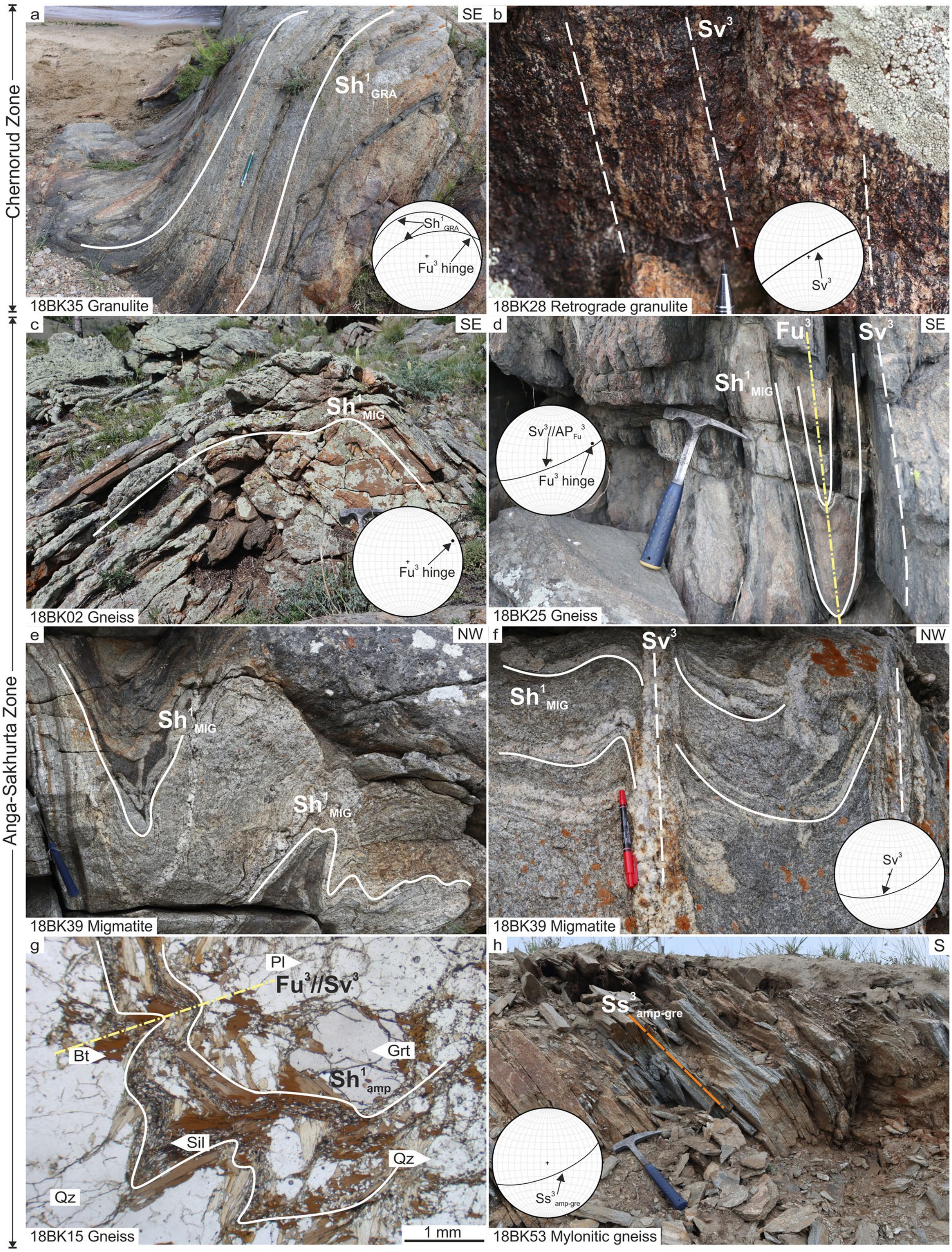
Chernorud Zone
Anga-Sakhurta Zone
a
SE
Sh^1_{GRA}
Sh^1_{GRA}
Fu^3 hinge
18BK35 Granulite
b
Sv^3
Sv^3
18BK28 Retrograde granulite
c
SE
Sh^1_{MIG}
Fu^3 hinge
18BK02 Gneiss
d
Fu^3
Sv^3
SE
Sh^1_{MIG}
$Sv^3//AP^3_{Fu}$
Fu^3 hinge
18BK25 Gneiss
e
NW
Sh^1_{MIG}
Sh^1_{MIG}
18BK39 Migmatite
f
Sv^3
NW
Sh^1_{MIG}
Sv^3
18BK39 Migmatite
g
Pl
$Fu^3//Sv^3$
Bt
Grt
Sh^1_{amp}
Sil
Qz
Qz
1 mm
18BK15 Gneiss
h
S
$Ss^3_{amp-gre}$
$Ss^3_{amp-gre}$
18BK53 Mylonitic gneiss

Figure 3.

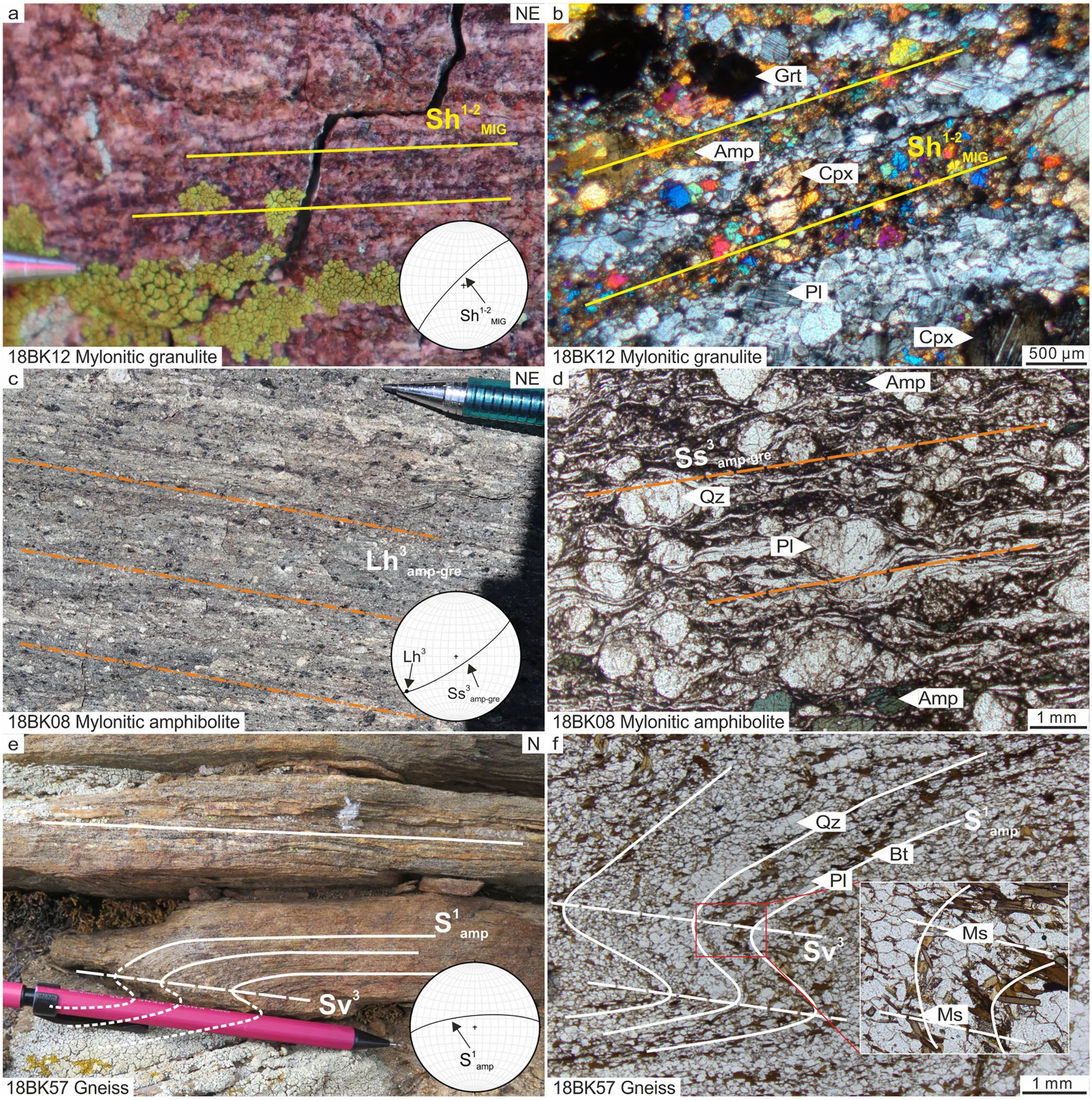

Figure 4. Petro-structural features of the mylonitic deformation zones in the Olkhon area: (a–b) high temperature mylonite zone from the northern part of the Chernorud Zone, showing dynamic recrystallization features of granulite characterized by sub-grain rotation recrystallization of plagioclase and pyroxene and syn-tectonic growth of amphibole. (c, d) Greenschist facies mylonitic zone affecting the Chernorud Zone, showing ultramylonitic microstructure with porphyroclasts of feldspars in association with dynamic recrystallization of plagioclase and amphibole forming ultra fine-grained groundmass. (e, f) Mylonitic gneiss from the Orso Complex characterized by extreme grain size reduction. Steep Fu^3 cleavage reworking S$^1_{amp}$ schistosity.

Figure 3. Representative field photographs and microphotographs showing the principal structural features of the Olkhon Terrane. (a, b) Chernorud Zone: (a) Sh$^1_{GRA}$ in layered mafic, intermediate, felsic granulite and gneiss are folded by open Fu^3 fold. (b) Mylonitic foliation in retrograde granulite marked by the alternated of amphibole-rich layers and plagioclase-quart-rich layers. (c–h) Anga-Sakhurta Zone: (c) Sh$^1_{MIG}$ foliation in gneiss folded by open Fu^3 fold. (d) Sh$^1_{MIG}$ foliation folded by isoclinal Fu^3 folds, causing penetrative reworking Sv^3 of the attenuated limbs. (e) Felsic, intermediate, and mafic migmatitic layering Sh$^1_{MIG}$ folded by open Fu^3 folds. (f) Felsic migmatite with apparent leucosomes parallel to Sh$^1_{MIG}$ foliation is folded by Fu^3 folds and affected by heterogeneously developed Sv^3 cleavage with Sv^3 parallel leucosome. (g) Sh$^1_{amp}$ foliation in a garnet-sillimanite gneiss marked by preferred orientation of biotite and folded by Fu^3 folds. (h) Strong mylonitic Ss$^3_{amp\text{-}gre}$ foliation reworking a gneiss.

(Figure 3b) and microstructural observations suggest that it is associated with dynamic recrystallization of the primary granulite facies assemblages (Figures 4a and 4b). The fine-grained plagioclase and K-feldspar indicate HT deformation (Figure 4b). The *P–T* conditions of relict granulite facies fabric were estimated to c. 8 kbar and 850°C and retrogression to ~6 kbar and 700°C in association with M^2_{amp} overprint (Z. Y. Li et al., 2023). The northern part of the Chernorud Zone is formed by an up to kilometer wide zone of amphibolite facies deformation reworking the granulite facies rocks, which is called the "collisional suture zone" in the Russian literature (Figure 2a) (Fedorovsky et al., 2020). The rocks inside the zone are folded by isoclinal upright folds, with steep hinges and axial planes parallel to the Siberian margin. Structural and microstructural observations indicate that some of these rocks are reworked by mylonites to ultramylonites that reveal dynamic recrystallization of quartz, feldspar and amphibole compatible with greenschist facies conditions (Figures 4c and 4d). Vertical foliation $Ss^3_{amp\text{-}gre}$ bears horizontal and strong stretching and mineral lineation $Lh^3_{amp\text{-}gre}$ (Figures 2g and 2h). Finally, all fabrics outside the amphibolite facies high strain zone, that is, the "collisional suture zone," are folded by meter to hundred meter-scale upright post-metamorphic Fu^3 folds with sub-horizontal hinges (Figures 2e and 3a).

The Anga-Sakhurta Zone, the subject of this study, is an amphibolite facies zone marked by numerous dome-like structures with migmatite-granite core and metamorphic envelope formed by layered quartzites, marbles, and amphibolites. The migmatite-magmatite domes form topographic highs of elliptic shapes while the metamorphic envelope occupies curved topographic depressions (Fedorovsky & Sklyarov, 2015). The long axes of these domal structures are generally parallel to the trend of the whole Anga-Sakhurta Zone even though there are examples where the domes have circular shapes. Fedorovsky (1997) and Fedorovsky and Sklyarov (2015) additionally showed that large domal structures are often formed by a number of sub-domes.

The central part of the migmatite-magmatite domain of the Anga-Sakhurta Zone was investigated in this study. An early sub-horizontal foliation Sh^1_{MIG} was observed in the gneissic granite, felsic stromatitic to nebulitic migmatite and sillimanite bearing paragneiss (Figures 3c–3f). This foliation was further folded by upright folds Fu^3 with sub-horizontal hinges (Figures 2e and 3c–3f). The folds vary from centimeters to meters scale but probably reach several hundred meters in wavelength and amplitude. They are open, close to isoclinal, with locally developed steep axial planar cleavage Sv^3 (Figure 3f). There are no new minerals associated with this cleavage but recrystallization of feldspars and biotite may indicate upper greenschist to lower amphibolite facies conditions (Figure 3g). Rarely, leucosome emplaced parallel to the axial planar foliation is discordant to the principal migmatite layering (Figure 3f). It is noteworthy that not only the principal layering (Figures 5c and 5g) but also horizontal leucocratic granite veins were affected by upright Fu^3 folding (Figures 5e and 5i). These features suggest that prior to Fu^3 folding the whole migmatite and granite edifice was disposed sub-horizontally. However, in some places the hinges of Fu^3 folds show steep plunges to the NE or SW which may imply moderate to steep dip of Sh^1_{MIG} prior to Fu^3 folding (Figure 5a). Our previous study (Z. Y. Li et al., 2023) revealed that the metamorphic cycle associated with the development of the Sh^1_{MIG} reached the P_{max} at 8 kbar at 770°C and was followed by a second phase of HT - low pressure (LP) metamorphism marked by M2 re-equilibration at around 4 kbar and 700°C. The structures related to this event are widely discussed and will be assigned as D^2_{MIG}.

The studied area is limited from the north by an orogen parallel shear zone (Figures 1 and 2a) where mylonitized granite sheets are steeply dipping to the south. A similar mylonitic zone also developed in the central part of the Anga-Sakhurta Zone, known as the "Main Shear Zone" (Figures 1 and 2a). These mylonitic zones are the latest structural feature and in analogy to Fedorovsky and Sklyarov (2015) or Vladimirov et al. (2011), they are assigned to a D3 event. The high strain zones are often associated with strong upper greenschist to lower amphibolite facies fabric $Ss^3_{amp\text{-}gre}$ (Figures 2g and 4d). From the south, the studied zone is limited by the strongly deformed Orso Complex which shows only NE-SW striking sub-vertical foliation defined by biotite, quartz, feldspar and garnet in paragneiss and/or micaschist (Figures 4f and 7h). In some places this metamorphic fabric bears steep lineation. This vertical fabric is likely a result of Fu^3 upright folding and incomplete transposition of the original S^1_{amp} or S^2_{amp} fabric by Sv^3 cleavage marked by growth of muscovite and biotite (Figures 4e and 4f). The D3 shearing is evidenced by a strong sub-horizontal lineation Lh^3_{myl} defined by intense stretching of all rock forming minerals (Figure 2h).

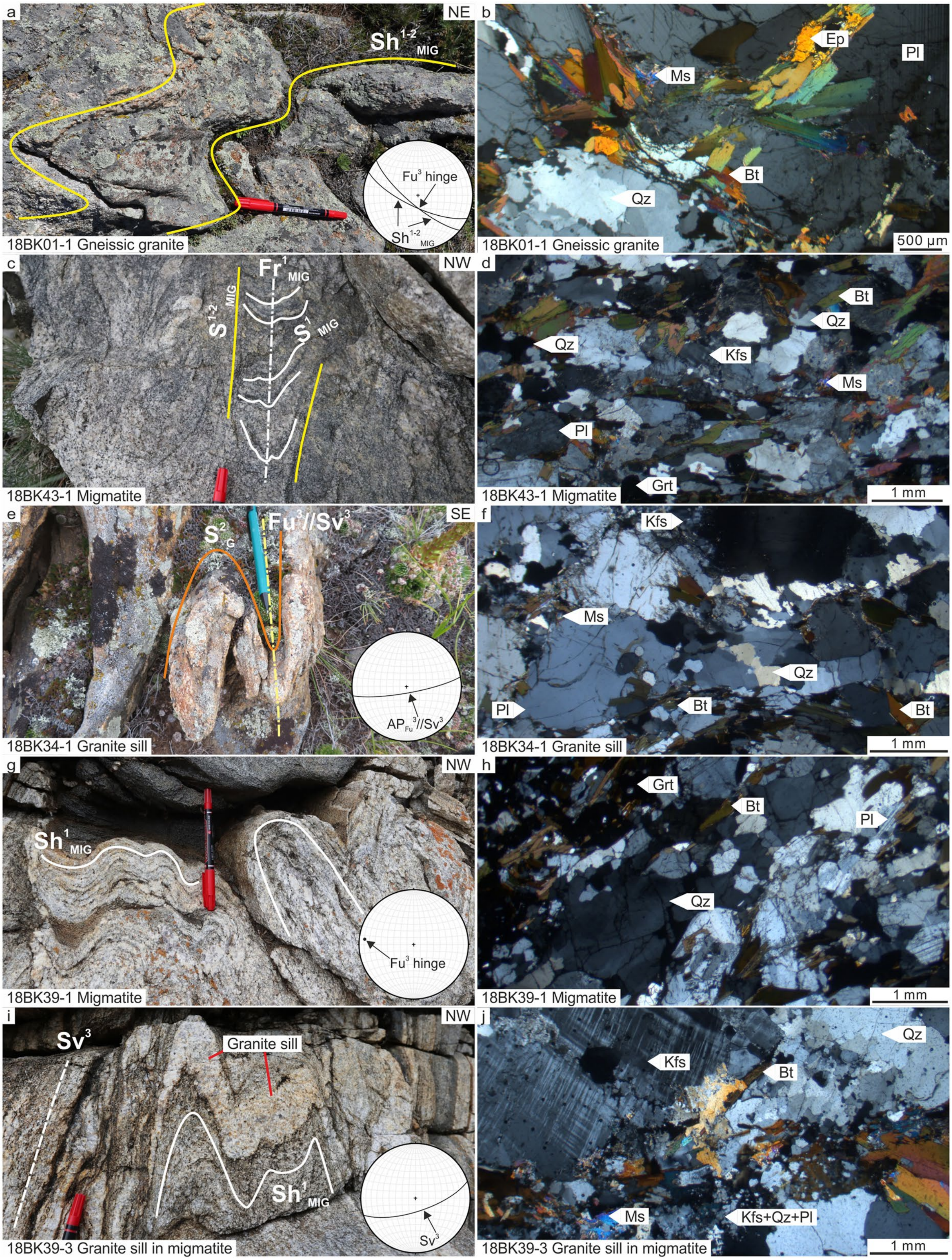
a
NE
Sh^{1-2}_{MIG}
Fu^3 hinge
Sh^{1-2}_{MIG}
18BK01-1 Gneissic granite
b
Ep
Pl
Ms
Bt
Qz
18BK01-1 Gneissic granite
500 μm
c
NW
Fr^1_{MIG}
S^{1-2}_{MIG}
S^1_{MIG}
18BK43-1 Migmatite
d
Bt
Qz
Qz
Kfs
Ms
Pl
Grt
18BK43-1 Migmatite
1 mm
e
SE
S^2_G
$Fu^3//Sv^3$
$AP_{Fu}^3//Sv^3$
18BK34-1 Granite sill
f
Kfs
Ms
Qz
Pl
Bt
Bt
18BK34-1 Granite sill
1 mm
g
NW
Sh^1_{MIG}
Fu^3 hinge
18BK39-1 Migmatite
h
Grt
Bt
Pl
Qz
18BK39-1 Migmatite
1 mm
i
NW
Sv^3
Granite sill
Sh^1_{MIG}
Sv^3
18BK39-3 Granite sill in migmatite
j
Qz
Kfs
Bt
Ms
Kfs+Qz+Pl
18BK39-3 Granite sill in migmatite
1 mm

Figure 5.

4. U-Pb Zircon Geochronology

Two samples, including a gneissic granite (18BK01-1) and a nebulitic migmatite (18BK43-1), from the Anga-Sakhurta Zone were collected for U-Pb zircon geochronological study. These samples are specifically selected for determining the age of basement, migmatization and granite emplacement within the Anga-Sakhurta Zone.

4.1. Analytical Methods

Zircon grains are extracted from the samples using standard heavy liquid and magnetic techniques, and then purified by hand picking under a binocular microscope. These grains were then fixed in epoxy resin and polished. An electron microprobe (JXA-8100, JEOL) equipped with a Mono CL3 cathodoluminescence (CL) system was used for imaging to record the internal zircon structure at the Guangzhou Institute of Geochemistry, Chinese Academy of Sciences (GIG, CAS). CL images of all analyzed zircon grains are provided in Figure S1.

Zircon U-Pb dating were analyzed by a GeolasPro laser ablation system that consisted of a COMPexPro102 ArF excimer laser (wavelength of 193 nm and maximum energy of 200 mJ) and a MicroLas optical system coupled with an Agilent 7700e ICP-MS at the Wuhan SampleSolution Analytical Technology (WSAT) Co., Ltd, following the analytical procedure described by Liu et al. (2008, 2010). The analysis was performed with a laser beam diameter of 32 μm. Zircon standard Harvard 91500 (Wiedenbeck et al., 1995) was used for calibration of the age data. Zircon standards GJ1 (601.92 ± 0.70 Ma, Jackson et al., 2004) and Plesovice (337.13 ± 0.37 Ma, Sláma et al., 2008) were used as monitors of the U-Pb dating. Over the process of analyses, the analyses on these monitoring standards gave weighted mean $^{206}Pb/^{238}U$ ages of 602 ± 3 Ma (MSWD = 0.011, $n = 10$) for GJ1 and 337 ± 2 Ma (MSWD = 0.027, $n = 4$) for Plesovice, which reproduced the recommended ages within analytical uncertainties. The mass fractionation correction and isotopic results for the analyses were calculated by ICPMSDataCal (version 11.2, Liu et al., 2010). Concordia diagrams and weighted mean calculations were made using Isoplot, all ages were presented and calculated with 2s in-run uncertainty (Ludwig, 2003). Analytical data are summarized in Table S1.

4.2. Results

4.2.1. Gneissic Granite Sample 18BK01-1

This sample was collected from the central doming region in the Anga-Sakhurta Zone (Figure 2a). The sample shows a steep granite fabric possibly steepened by upright fold Fu^3, defined by alternating bands of plagioclase-rich and biotite-rich layers. The foliation has been folded by Fu^3 which are SW-NE trending and show vertical hinges (Figure 5a). The gneissic granite is composed of plagioclase, quartz, biotite, and epidote. Plagioclase and quartz crystals are 0.5–5 mm in diameter. Fine-grained quartz crystals developed around coarse plagioclase/quartz crystals. Biotite is present as irregular shaped flakes developed between main porphyroclasts. Sparse garnet and epidote crystals are 0.1–0.3 mm in diameter (Figure 5b).

Zircons from this sample are predominantly euhedral and subhedral ranging from 100 to 300 μm in longest axis (Figure S1). Individual zircon grains often contain rounded to irregular shaped CL-bright cores, where oscillatory or sector zoning patterns can occasionally be observed. Associated zircon rims are CL-dark with faint oscillatory to homogeneous zoning patterns. Rarely, zircon cores resemble the zircon rims but with an irregular boundary separating the two domains. Both zircon cores and rims have been targeted for U-Pb analysis, yielding a bimodal distribution of ages (Figures 6a and 6b). Concordant analyses of CL-bright zircon cores ($n = 15$) yielded Paleoproterozoic ages (c. 2,051–2,226 Ma) with a weighted mean $^{207}Pb/^{206}Pb$ age of 2,143 ± 24 Ma (MSWD = 1.6). Concordant analyses from the CL-dark zircon rims ($n = 12$) yielded individual ages from 440 to 469 Ma with a weighted mean $^{206}Pb/^{238}U$ age of 452 ± 3 Ma (MSWD = 3.0) (Figure 6b). Considering also discordant analyses, a discordia line is calculated

Figure 5. Representative field photographs and photomicrographs of samples selected for zircon and monazite U-Pb dating. Gneissic granite 18BK01-1: (a) Foliation in gneissic granite folded by Fu^3 asymmetric fold, (b) coarse-grained crystals are affected by D3 deformation leading to dynamic recrystallization of quartz and brittle deformation of feldspar. Migmatite 18BK43-1: (c) Schlieren to nebulitic migmatite, in which the S^1_{MIG} schlieren fabric is folded by rootless Fr^1_{MIG} folds, while, in other places, it is completely transposed by ubiquitous migmatitic foliation S^{1-2}_{MIG}, (d) coarse-grained S^1_{MIG} foliation defined by elongation of quartz and feldspar, and preferred orientation of biotite. Superimposed is weak solid-state D3 reworking defined by quartz dynamic recrystallization reducing the grain size. Leucocratic granite sills 18B34-1: (e) Leucogranite vein folded by isoclinal Fu^3 folds, (f) coarse-grained microstructure of vein defined by biotite preferred orientation, feldspar elongation, and dynamically recrystallized quartz bands. The latter feature is probably related to D3. Banded to schlieren migmatite 18BK39-1: (g) Sh^1_{MIG} folded by open to closed Fu^3 folds, (h) coarse-grained Sh^1_{MIG} foliation defined by biotite preferred orientation, and feldspar and quartz elongation. Granite sill in migmatite 18BK39-3: (i) Low strain domain in layered migmatite with granite sill parallel to the Sh^1_{MIG} foliation, folded by open to isoclinal Fu^3 folds, (j) magmatic microstructure defined by coarse-grained biotite, quartz, and feldspar. Superimposed is solid-state deformation leading to fine-grained recrystallization of quartz, feldspars, and muscovite.

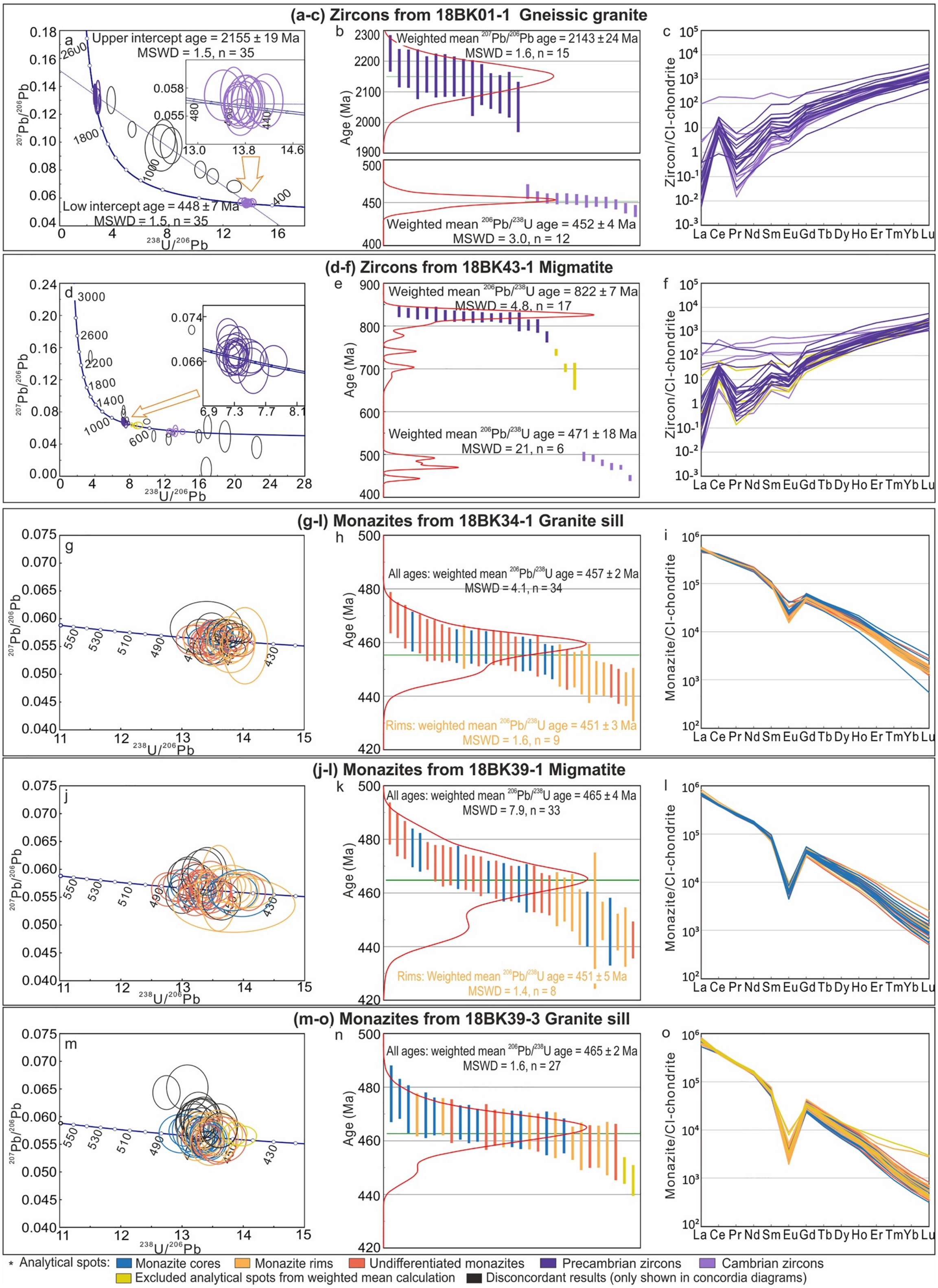

Figure 6. (a–f) Representative zircon U-Pb concordia diagrams, age bar plots and REE patterns. (g–o) Representative monazite U-Pb concordia diagrams, age bar plots and REE patterns. The interpretation of zircon ages was based on ^{206}Pb/^{238}U ages for grains <1,000 Ma and on ^{207}Pb/^{206}Pb ages for grains >1,000 Ma.

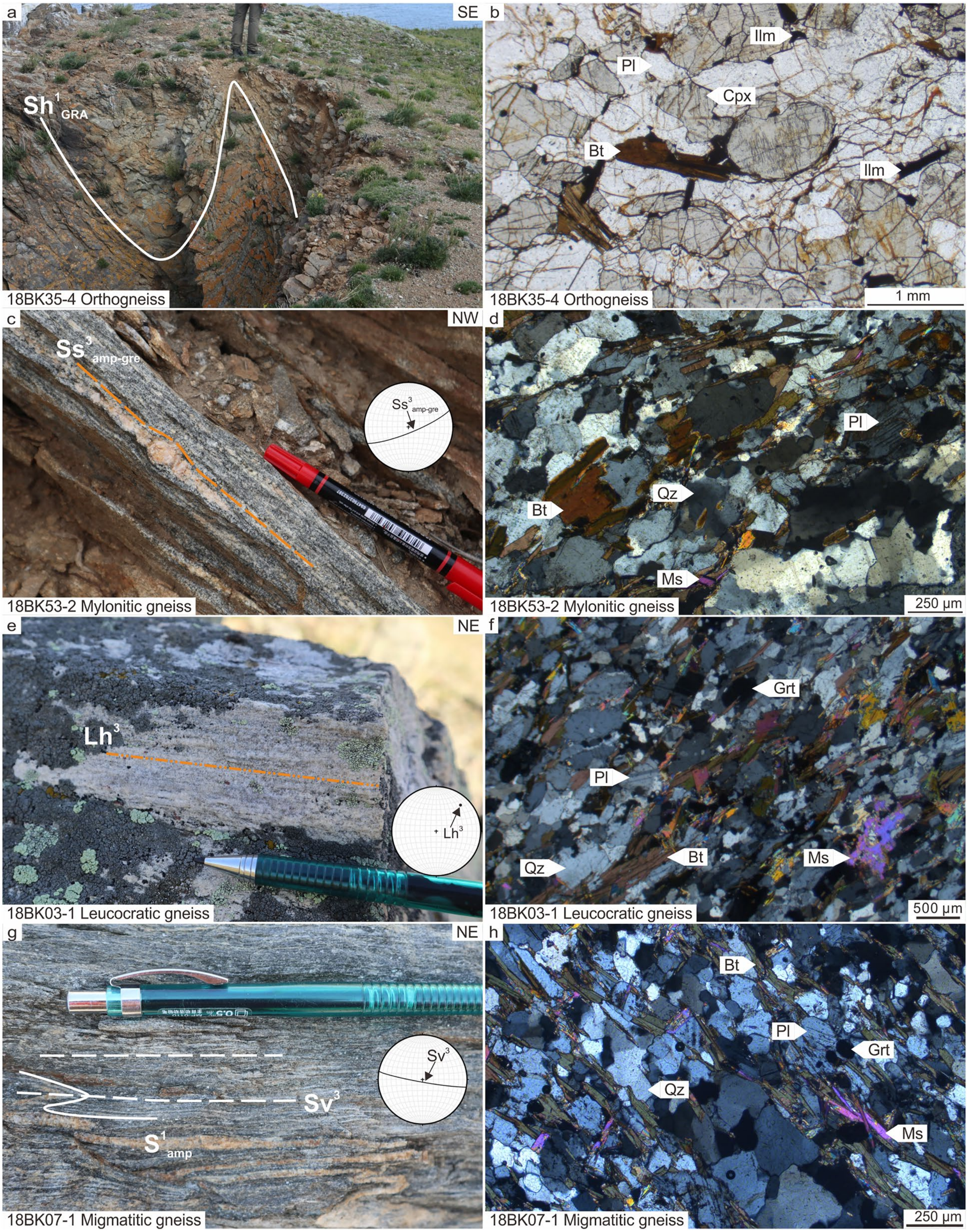
a
SE
Sh^1_{GRA}
18BK35-4 Orthogneiss
b
Ilm
Pl
Cpx
Bt
Ilm
18BK35-4 Orthogneiss
1 mm
c
NW
$Ss^3_{amp-gre}$
$Ss^3_{amp-gre}$
18BK53-2 Mylonitic gneiss
d
Pl
Qz
Bt
Ms
18BK53-2 Mylonitic gneiss
250 μm
e
NE
Lh^3
Lh^3
18BK03-1 Leucocratic gneiss
f
Grt
Pl
Bt
Ms
Qz
18BK03-1 Leucocratic gneiss
500 μm
g
NE
Sv^3
Sv^3
S^1_{amp}
18BK07-1 Migmatitic gneiss
h
Bt
Pl
Grt
Qz
Ms
18BK07-1 Migmatitic gneiss
250 μm

Figure 7.

with upper intercept at 2,155 ± 19 Ma and a lower intercept at 448 ± 7 Ma and an MSWD value of 1.5 (Figure 6a). The Th/U ratios of zircon cores yielded mostly moderate to high values (0.19–0.87, with additional outliers at 0.02 and 1.43), whereas the zircon rims yielded uniformly low values (0.06–0.15 except for one outlier at 0.40). The REE contents of the zircon cores and rims broadly overlap (Figure 6c), but zircon rims exhibit generally higher Gd/Yb ratios (0.03–0.09 except for one outlier at 0.12) than the zircon cores (0.03–0.04 except for two outliers at 0.10).

4.2.2. Nebulitic Migmatite Sample 18BK43-1

The nebulitic migmatite (18BK43-1) was sampled from the southwest bank of the Olkhon Island, and belongs to the southern part of the Anga-Sakhurta Zone (Figure 2a). Stromatitic layering S^1_{MIG} is defined by well-developed biotite-rich schlieren and the local occurrence of patchy leucosomes (Figure 5c). The S^1_{MIG} schlieren fabric is folded by rootless Fr^1_{MIG} folds, while, in other places, it is completely transposed by ubiquitous migmatitic foliation S^{1-2}_{MIG} in the host diatexite. This site is a rare example where Fr^1_{MIG} folds can be observed but the original attitudes of the S^1_{MIG} cannot be determined at the given outcrop. The sample consists of plagioclase, quartz, K-feldspar, biotite, muscovite, and garnet. In thin-section, the feldspar and quartz crystals are ranging from 0.2 to 2 mm in diameter (Figure 5d). Orientation of biotite-rich domains defines the migmatitic fabric. Muscovite forms rare small and irregular shaped grains. Garnet is relatively fine-grained with maximum diameter of 0.5 mm, and is present in both biotite-rich and plagioclase-rich domains (Figure 5d).

Zircons from this sample are anhedral to subhedral, ranging from 70 to 200 μm in the longest axis. Most zircon grains exhibit contrasting core and rim domains. The cores are typically brighter in CL image and have irregular, oscillatory, or sector zoning while the rims are CL-dark and homogeneous (Figure S1). Individual analysis yielded a range of concordant ages from 444 to 837 Ma (Figures 6d and 6e). A relatively coherent older group ($n = 17$), sampled exclusively from zircon cores yielded a weighted mean $^{206}Pb/^{238}U$ age of 822 ± 7 Ma (MSWD = 4.8) (Figure 6e). Three additional analyses on zircon cores yielded concordant ages between 741 and 684 Ma and six concordant analyses on CL-dark zircon rims yielded ages between 495 and 444 Ma with a poorly defined weighted mean $^{206}Pb/^{238}U$ age of 471 ± 18 Ma (MSWD = 21) (Figure 6e). The U contents of these zircon rims are notably higher (837–2,257 ppm) compared to the zircon cores (69–783 ppm, and one outlier at 1,858 ppm) and four of the zircon rim analyses are noted for high content of light-REE (Figure 6f). Additionally, several analyses targeted at zircon rims ($n = 14$) with extreme high U contents (up to 7,723 ppm) yielded discordant data points with $^{206}Pb/^{238}U$ ages varying from 499 to 37 Ma.

5. U-Pb Monazite Geochronology

Three samples from the Anga-Sakhurta Zone have been analyzed by monazite U-Pb geochronology. Two samples represent leucocratic granitic sills (18BK34-1, 18BK39-3), which intrude the migmatite fabric S^1_{MIG} and were folded during Fu^3 upright folding. As the granite veins intruded as sills into pre-existing fabric, their fabrics are assigned as S^2_G. An additional sample is from the migmatite host rock (18BK39-1) of one of the leucocratic granitic sills. These samples were targeted for geochronological study to constrain the relative timing of development of S^2_G fabric and possibly late melt crystallization event related to Fu^3 in the Anga-Sakhurta Zone.

5.1. Analytical Methods

Monazite grains are extracted from the samples using the same method as zircon grains, and using the same machine to obtain the back-scattered electrons (BSE) images at the GIG, CAS. BSE images of all analyzed grains are provided in Figure S1. The LA-ICP-MS U-Pb analysis of monazites were carried at the WSAT Co., Ltd in the same method as the analysis of zircon grains, but the diameter of the laser beam for monazite analysis is 16 μm.

Monazite standard USGS-44069 (Aleinikoff et al., 2006; Richter et al., 2019) and glass NIST610 were used as external standards for U-Pb age dating and trace element calibrations. The monazite standard Trebilcock (TRE) (272 ± 4 Ma, Tomascak et al., 1996) was employed as secondary standard, which gave a weighted

Figure 7. Representative field photographs and photomicrographs of samples for biotite $^{40}Ar/^{39}Ar$ dating. Orthogneiss 18BK35-4: (a) The Sh^1_{GRA} foliation is folded by Fu^3 fold with a sub-horizontal hinge, (b) the rock consists of clinopyroxene, biotite, plagioclase, and minor ilmenite, biotite is ∼1 mm in size. Mylonitic gneiss 18BK53-2: (c) Feldspar porphyroclast elongated and parallel to mylonitic foliation $Ss^3_{amp-gre}$, (d) recrystallized biotite, plagioclase, quartz, and muscovite matrix with grains elongated parallel to the $Ss^3_{amp-gre}$. Leucocratic gneiss 18BK03-1: (e) Strong sub-horizontal stretching lineation Lh^3, (f) quartz and plagioclase developed dynamically recrystallized matrix, muscovite and biotite shows strong shape preferred orientation. Migmatitic gneiss 18BK07-1: (g) Sv^3 foliation defined by the transposition of quartz-feldspar-rich and biotite-rich fabric S^1_{amp}, which is isoclinally folded, (h) biotite and muscovite show strong shape preferred orientation, plagioclase, and quartz show subhedral shapes with straight boundaries.

mean $^{206}Pb/^{238}U$ age of 270 ± 2 Ma (MSWD = 0.2, $n = 6$) over the period of the analyses. The mass fractionation correction and isotopic results for the analyses were calculated by ICPMSDataCal (version 11.2, Liu et al., 2010). Concordia diagrams and weighted mean calculations were made using Isoplot, and all individual ages were presented and calculated with 2s in-run uncertainty (Ludwig, 2003). Analytical data are summarized in Table S1.

5.2. Results

5.2.1. Granite Sill Sample 18BK34-1

Granite sill sample 18BK34-1 was collected from an outcrop in the southern part of the Anga-Sakhurta Zone (Figure 2a). The sill has been folded by upright isoclinal fold Fu^3, and limbs of fold were completely transposed to Sv^3 with subvertical dip (Figure 5e). The sample is composed of plagioclase, quartz, K-feldspar, biotite and minor muscovite (Figure 5f). The plagioclase and quartz crystals are 1–2 mm in size. The quartz forms recrystallized and elongate aggregates with straight and lobate boundaries aligned parallel to the principal foliation. Biotite grains are strongly oriented and aligned parallel to the S^2_G. Fine-grained muscovite occurs occasionally.

Monazite grains from this sample are subhedral to anhedral and range from 90 to 200 μm in diameter. Most grains exhibit a faint zoning in BSE images with darker core surrounded by slightly lighter rim, however a few grains are homogeneous (Figure S1). Individual analysis yielded a continuous spread of $^{206}Pb/^{238}U$ ages between 444 and 472 Ma (Figures 6g and 6h). A weighted mean $^{206}Pb/^{238}U$ age calculated from the full data set ($n = 34$) yielded an age of 457 ± 2 Ma, with a relatively large MSWD value (4.1). Analyses from unambiguous monazite rims ($n = 9$) according to the BSE images (Figure S1) yielded a tighter population (MSWD = 1.6) with a weighted mean $^{206}Pb/^{238}U$ age of 451 ± 3 Ma (Figure 6g). There is however no systematic variation in the monazite REE chemistry with age; all analyses display similar right-dipping REE patterns with moderate negative Eu anomalies and a constant Yb/Gd ratio of 0.04–0.06 (Figure 6i).

5.2.2. Leucocratic Migmatite Sample 18BK39-1

Sample 18BK39-1 was collected from the leucosome of a stromatitic migmatite outcrop on the west bank of the Olkhon Island, in the northern part of the Anga-Sakhurta Zone (Figure 2a). The outcrop shows a well-developed sub-horizontal foliation Sh^1_{MIG} which is defined by typical stromatitic layering (Figure 5g). The layering was folded by open upright folds Fu^3 with steep axial planes and sub-horizontal hinges. The sample is composed of garnet, quartz, plagioclase, and biotite. The garnet porphyroblasts with biotite and quartz inclusions are ~0.5 mm in size and often fractured. Plagioclase and quartz grains are ~1 mm in diameter. Biotite crystals underline the stromatitic layering parallel to S^1_{MIG} (Figure 5h).

Monazite grains from sample 18BK39-1 are anhedral and often fractured or broken, and the sizes of individual monazite grains vary from 100 to 250 μm. Patchy zoning patterns in BSE image dominate and only a few grains exhibit clear core (BSE-light) and rim (BSE-dark) domains (Figure S1). The analyses yielded a significant spread of ages between 442 and 486 Ma (Figures 6j and 6k). A weighted mean $^{206}Pb/^{238}U$ age calculated from the complete data set yielded an age of 465 ± 4 Ma ($n = 33$), but the high MSWD value (7.9), implies that it is not a coherent population. Eight analyses performed on unambiguous monazite rims in BSE image (Figure S1) yielded a weighted mean $^{206}Pb/^{238}U$ age of 451 ± 5 Ma with MSWD value of 1.4 (Figure 6k). Nonetheless, the monazite REE contents again show no significant variation with age and is characterized by right-dipping REE patterns with pronounced negative Eu anomalies and a constant Yb/Gd ratio of 0.02–0.05 (Figure 6l).

5.2.3. Granite Sill Sample 18BK39-3

Sample 18BK39-3 is a granite sill from the same locality as sample 18BK39-1 (Figure 2a). The granite is parallel to the stromatitic layering Sh^1_{MIG} of the migmatite host rock and is folded by upright open folds Fu^3 (Figure 5i). This rock consists of plagioclase, quartz, K-feldspar, biotite, and muscovite (Figure 5j). Plagioclase, K-feldspar and quartz crystals are coarse grained, up to ~10 mm in size. Quartz exhibits undulose extinction and signs of dynamic recrystallization, and recrystallized quartz/pressure-solution fabric can be observed. Fine-grained K-feldspar, plagioclase, and quartz assemblage are also developed in the matrix with muscovite and biotite. Biotite additionally occurs around feldspar porphyroclasts but is only distributed in less than 5% total volume in this sample. Muscovite is observed as residual fabric with fine-grain minerals.

Monazite grains from the sample are subhedral to anhedral and range from 80 to 200 μm in the longest axis. Most grains show clear core and rim zoning in BSE images (Figure S1); the monazite cores are BSE-light and homogeneous, while the rims are darker and exhibit faint patchy to oscillatory zoning. The analyses produce a relatively continuous spread of ages between 445 and 478 Ma with a weighted mean ^{206}Pb/^{238}U age of 465 ± 2 Ma (MSWD = 1.6, n = 27) (Figures 6m and 6n). This weighted mean is not improved by considering only the unambiguous monazite rims from BSE images (Figure S1). Note as well that the two youngest analyses were excluded from this weighted mean as statistical outliers. These two analyses are also noted for higher Yb/Gd ratios (0.08 and 0.10) than the main population (0.02–0.03) (Figure 6o), further justifying their exclusion.

6. Biotite ^{40}Ar/^{39}Ar Geochronology

Four representative samples from each of the principal zones of the Olkhon Terrane were analyzed by the ^{40}Ar/^{39}Ar stepwise heating of biotite (Figure 2a). A folded orthogneiss (18BK35-4) was sampled from the southern boundary of the Chernorud Zone with the Anga-Sakhurta Zone; a mylonitic gneiss (18BK53-2) was sampled from the Main Shear Zone in the central part of the Anga-Sakhurta Zone; a leucocratic gneiss (18BK03-1) was sampled from the main doming region in the southern part of the Anga-Sakhurta Zone; and a felsic gneiss (18BK07-1) was sampled close to the boundary between the Orso Complex and the Anga-Sakhurta Zone. These samples were targeted for analysis to date the cooling of the Olkhon Terrane after Fu^3 folding and the D3 mylonitic shear deformation.

6.1. Analytical Methods

Hand-specimens were individually crushed and sieved to 30–60 mesh, then the biotite minerals were separated by hand picking under a binocular microscope and cleaned by ultrasonic with deionized water. The samples were individually wrapped in aluminum foil and the flux monitor ZHB-25 biotite was wrapped in copper foil. The samples and monitors were put into aluminum tubes then irradiated for 48h in the Beijing 49-2 reactor The biotite standard of ZBH-25 (the Fangshan granodiorite) has a ^{40}Ar/^{39}Ar plateau age of 132.7 ± 0.1 Ma (1s, Wang, 1983). Previous calibrations of this standard against several representative laboratory standards, including the GA1550 and LP-6, attested it as a suitable ^{40}Ar/^{39}Ar age reference material (Sang et al., 2006).

Samples 18BK03-1 and 18BK35-4 were analyzed at the GIG, CAS, and samples 18BK07-1 and 18BK53-2 were analyzed at the Key Laboratory of Tectonics and Petroleum Resources, China University of Geosciences, Wuhan (CUG, Wuhan). The ^{40}Ar/^{39}Ar laser heating analysis in both two laboratories were carried-out using a 50W CO_2 laser, the released gases were purified through cryotrap and Zr/Al getters, then analyzed by Thermo Scientific©ARGUS VI mass spectrometer, the detailed analytical methods are described in Bai et al. (2018) and Zhang et al. (2021). The ZBH-25 biotite standard was analyzed to monitor the neutron flux in both laboratories. All the ^{40}Ar/^{39}Ar analyses data were calculated and plotted using the ArArCalc software package with 2s in-run uncertainty (Koppers, 2002). The J-value of each sample was interpolated based on the regression line of J-values of measured monitor standards. The total decay constant for ^{40}K used is $k = 5.530 \times 10^{-10}$/yr from Renne et al. (2010), and the correction factors used for interfering argon isotopes derived from irradiated CaF_2 and K_2SO_4 are: $(^{39}\mathrm{Ar}/^{37}\mathrm{Ar})_{\mathrm{Ca}} = 6.175 \times 10^{-4}$, $(^{36}\mathrm{Ar}/^{37}\mathrm{Ar})_{\mathrm{Ca}} = 2.348 \times 10^{-4}$, and $(^{40}\mathrm{Ar}/^{39}\mathrm{Ar})_{\mathrm{K}} = 2.323 \times 10^{-3}$. Uncertainties of the ^{40}Ar/^{36}Ar ages were reported at the 2s level. Analytical data are summarized in Table S2. In this study, at least 5 or more consecutive steps (consistent at 95% confidence level) that contain >70% the cumulative ^{39}Ar released is used to define a plateau, and 50%–70% and <50% of the cumulative ^{39}Ar released are used to define a mini-plateau and pseudo-plateau, respectively (Hénocque et al., 1998; Jourdan et al., 2007; Schaen et al., 2021). A standard air ^{40}Ar/^{36}Ar ratio of 298.56 (Lee et al., 2006) was applied to the calibration on radiogenic argon, since the extremely high radiogenic Ar with respect to the atmospheric Ar of the biotite samples makes precise determination of initial ^{40}Ar/^{36}Ar ratio difficult. Yet, it has been suggested that the initial ^{40}Ar/^{36}Ar ratio has little influence on the ^{40}Ar/^{39}Ar ages of K-enriched minerals (e.g., biotite, Bachmann et al., 2010; Clay et al., 2011).

6.2. Results

6.2.1. Pyroxene-Bearing Orthogneiss 18BK35-4

The sample was collected from the granulite-facies Chernorud Zone (Figure 2a). Foliation Sh^1_{GRA} is formed by compositional layering marked by alternations of felsic-rich and mafic-rich bands. The Sh^1_{GRA} has been folded by Fu^3 fold with a steep axial plane and a sub-horizontal hinge (Figure 7a). The analyzed sample was taken from the hinge zone of the Fu^3 fold. This sample is composed of clinopyroxene, plagioclase, biotite and minor ilmenite (Figure 7b).

The biotite from this sample was analyzed in 10 incremental heating steps. The first two steps and the last step yield discordant apparent ages below 400 Ma, and steps 3–9 yield a flat age spectrum which constrains a well-defined plateau age of 408.4 ± 1.2 Ma (MSWD = 1.47) covering 78.8% of ^{39}Ar release (Figure 8a). These steps also form a normal isochron with an age of 410.3 ± 1.9 Ma (MSWD = 0.62) (Figure 8b), which agrees with the plateau age.

6.2.2. Mylonitic Gneiss 18BK53-2

Sample 18BK53-2 was collected from the Main Shear Zone in the Anga-Sakhurta Zone (Figure 2a). The sample shows mylonitic layering defining the vertical foliation $Ss^3_{amp\text{-}gre}$ (Figure 7c). In thin section, dynamically recrystallized plagioclase, quartz, biotite and muscovite form an equigranular matrix (Figure 7d). Recrystallized plagioclase grains are ranging from 200 to 500 μm in diameter and are elongated and aligned parallel to the $Ss^3_{amp\text{-}gre}$ foliation. Quartz is 200 μm to 2 mm in size and shows features compatible with moderate mobility of grain boundaries and presence of sub-grains. Biotite shows strong shape preferred orientation parallel to the $Ss^3_{amp\text{-}gre}$ foliation.

Biotite from this sample was analyzed in 18 incremental heating steps. The apparent ages obtained from the low-temperature steps form an increasing age spectrum with the apparent age increasing from 325 to 395 Ma. In contrast, the last nine continuous steps give uniform apparent age forming a mini-plateau with age of 401.1 ± 2.2 Ma (MSWD = 0.28) covering nearly 57.5% of ^{39}Ar release (Figure 8c). The related steps also form a normal isochron with a calculated age of 402.2 ± 3.2 Ma (MSWD = 0.21) (Figure 8d), which agrees with the mini-plateau age.

6.2.3. Leucocratic Mylonitic Gneiss Sample 18BK03-1

The sample is from the southern part of the Anga-Sakhurta Zone (Figure 2a). The rock shows vertical foliation Sv^3 and strong horizontal lineation Lh^3 at the outcrop (Figure 7e). The sample is composed of recrystallized K-feldspar, plagioclase, quartz, biotite and rare muscovite and garnet (Figure 7f). Biotite is strongly oriented forming the dominant Sv^3 foliation with dynamically recrystallized quartz and plagioclase grains up to ∼0.5 mm in diameter.

Stepwise heating of biotite from this sample yields similar apparent ages ranging from 387 to 408 Ma. A flat age spectrum defined by the last eight steps (covering 96.5% of total ^{39}Ar release) yields a plateau age of 406.1 ± 1.2 Ma (MSWD = 0.95, Figure 8e), which agrees with the normal isochron age of 408.6 ± 3.6 Ma (MSWD = 0.73) (Figure 8f).

6.2.4. Felsic Gneiss Sample 18BK07-1

This sample is a strongly deformed felsic gneiss collected from the Orso Complex (Figure 2a). The rock is composed of garnet, biotite, muscovite, plagioclase and quartz. At the outcrop the rock shows vertical foliation Sv^3 defined by the alternation of isoclinally folded quartz-feldspar-rich and biotite-rich layers (Figure 7g). These relations indicate strong transposition of older S^1_{amp} metamorphic fabric. Fine-grained garnet grains ∼100 μm in diameter are euhedral to subhedral in shape. Plagioclase and quartz, 100–300 μm in size, show characteristic subhedral shapes with straight boundaries sometimes meeting at triple points. Biotite and muscovite show strong preferred orientation parallel with macroscopic foliation Sv^3 (Figure 7h).

Biotite from this sample was analyzed in 19 incremental heating steps. Steps 1–8 yield increasing apparent age from 336 to 416 Ma, whereas steps 9–19 yield coherent apparent ages defining an age plateau at 420.9 ± 2.3 Ma (MSWD = 0.31) (Figure 8g). This plateau covers 71.4% of total ^{39}Ar release. The related data points also from a well-defined normal isochron with an age of 421.6 ± 2.6 Ma (MSWD = 0.15) (Figure 8h).

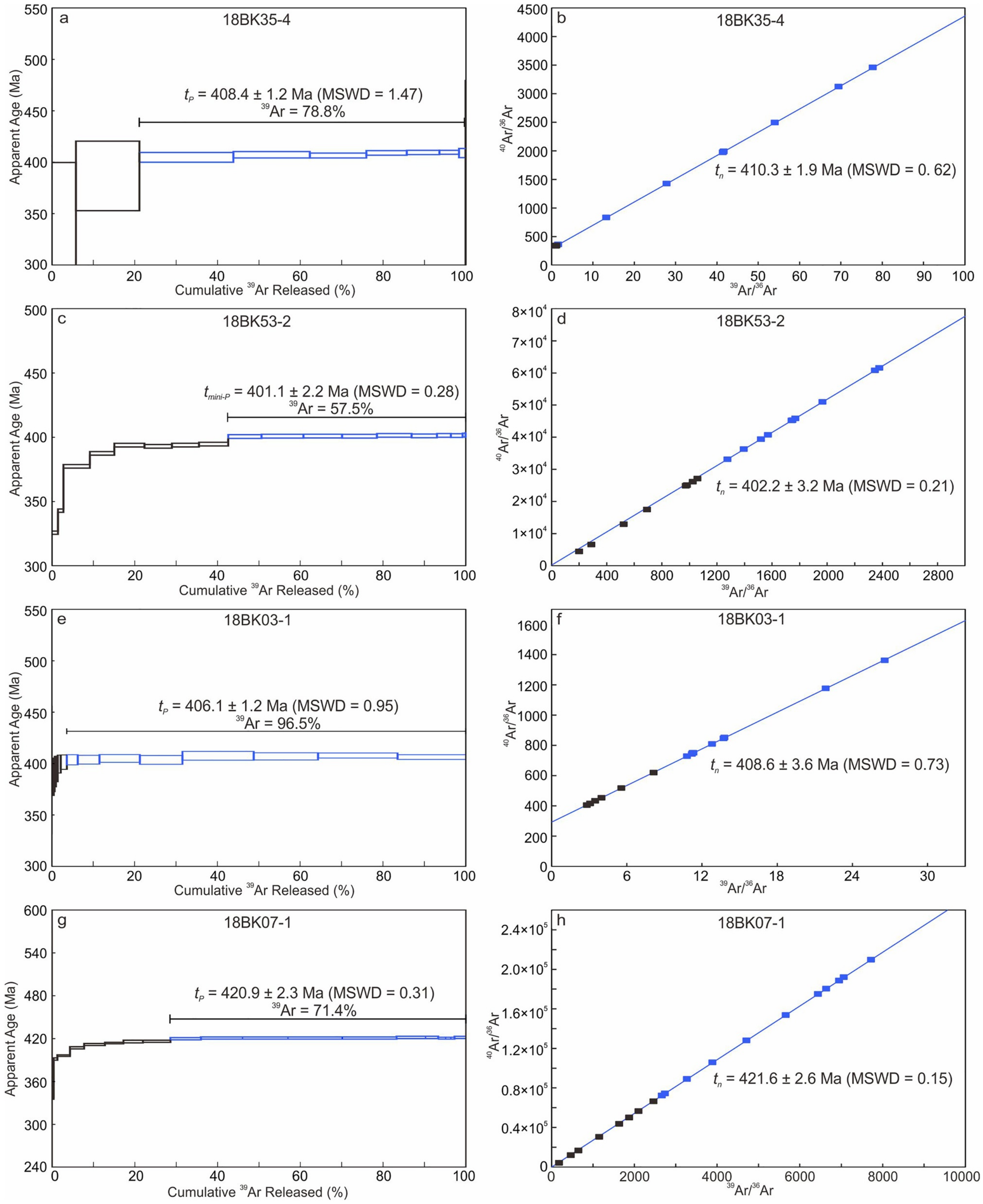

Figure 8. Age spectra and normal isochrons of biotite ^{40}Ar/^{39}Ar age dating. The black spots in normal isochrons represent steps that are excluded from the calculations of plateau ages and normal isochrons ages.

7. Discussion

7.1. Significance of Horizontal Metamorphic Fabrics of the Anga-Sakhurta Zone

This study shows that the earliest metamorphic fabric in the studied migmatite and gneiss is the Sh^1_{MIG} fabric parallel to leucosomes in stromatic to nebulitic migmatite but also parallel to orientation of leucogranite sills (Figures 3 and 5). There are also occasional vertical granite veins emplaced parallel to the axial planes of Fu^3 folds (Figure 3f). Hinges of these folds are plunging either NE or SW mainly under shallow angles but occasionally also steep angles (Figures 2e and 5a). These features imply that the Sh^1_{MIG} was mainly sub-horizontal, but in some places was dipping to the NE or SW under moderate to steep angles. Such distribution of the fabric may indicate two possible geometrical origins: (a) the S^1_{MIG} was originally sub-horizontal and folded prior to D3 by upright folds with hinges and axial planes oriented at high angle to Fu^3 folds or, (b) the verticalization of the S^1_{MIG} and sub-horizontal granite veins prior to the Fu^3 folding was related to more or less isometric doming. In both cases, folding or doming affected the Sh^1_{MIG} and granite sheets after their formation and we can, together with other authors (e.g., Dobrzhinetskaya et al., 1992; Fedorovsky, 1997; Fedorovsky & Sklyarov, 2015), assume that the S^1_{MIG} was primarily sub-horizontal.

Sub-horizontal metamorphic fabric in orogens is a common feature and is explained either as related to nappe stacking associated to recumbent folding as is the case in Olkhon Terrane tectonic models (Fedorovsky, 1997 and many others), horizontal channel flow in large hot orogens (e.g., Beaumont et al., 2006), horizontal syn-extensional flow (e.g., Cosgrove, 1997; Y. D. Jiang et al., 2019; Kong et al., 2022), or extensional collapse of thickened orogens associated with the development of migmatite core complexes (e.g., Vanderhaeghe & Teyssier, 2001). The key element is the metamorphic history associated with the horizontal fabric, which shows HP (high pressure) to MP (middle pressure) metamorphic gradients and typical clockwise $P–T$ loop with P_{max} preceding T_{max} in nappe-stacking or channel flow models (Jamieson et al., 2002). In contrast, syn-extensional flow or extensional collapse is generally connected with LP metamorphic gradient and sometimes also with an anticlockwise $P–T$ loop (Rey et al., 2009; Thompson et al., 2001).

Our previous study (Z. Y. Li et al., 2023) showed that garnet-sillimanite bearing paragneiss in the region recorded a two-stage metamorphic $P–T$ evolution (Figure 9a). The early burial and heating to maximum conditions of ~8 kbar at 770°C (M1) was subsequently followed by decompression with limited cooling to ~4 kbar at 670°C (M2). Petrochronological data further indicated that the M1 event occurred at c.500 Ma while the second M2 event occurred at c. 450 Ma (Z. Y. Li et al., 2023). Based on these results, it has been proposed that the original Sh^1_{MIG} fabric of the Anga-Sakhurta Zone together with granulite fabric Sh^1_{GRA} in the Chernorud Zone resulted from moderate crustal thickening. These data are in agreement with a generally accepted model for the region of nappe stacking and recumbent Fr^1 folding resulting in crustal thickening (e.g., Donskaya et al., 2013; Fedorovsky & Sklyarov, 2015). These isoclinal, sometimes rootless and non-cylindrical sheath-like recumbent folds are typical for hot fold nappe architecture developed during paroxysmal stages of hot collisional orogens worldwide (e.g., Jamieson & Beaumont, 2013; Schulmann et al., 2008).

Hypothetically, the horizontal granite veins (sills) studied in this work can intrude the pre-existing Sh^1_{MIG} horizontal anisotropy during an independent tectonic event. If this happened during M2 pressure drop, then it should be related to an extensional event following the collision or orogenic collapse (e.g., Vanderhaeghe & Teyssier, 2001). Under such conditions the granitoids emplaced in the interval 480–460 Ma in the migmatitic Anga-Sakhurta Zone should have the form of sub-horizontal or gently inclined sheets (e.g., Améglio et al., 1997; Faure & Pons, 1991) or domal structures if the emplacement of granite was assisted with buoyancy driven flow (e.g., Kruckenberg et al., 2010; Vanderhaeghe et al., 2004). The other important factor was the existence of horizontal Sh^1_{MIG} mechanical anisotropy. If the syn-D2 differential stress (vertical principal compressive stress) was lower compared to ratio of tensional strength parallel and perpendicular to the mechanical anisotropy, then granitoids have to emplace in the form of sills parallel to the main horizontal fabric (Cosgrove, 1997). The geochronology study of migmatite and granitic veins with well-constrained Sh^1_{MIG} and granite sheets is therefore of paramount importance to assess the complete tectono-thermal history of the Olkhon Terrane and it will be discussed in following paragraphs.

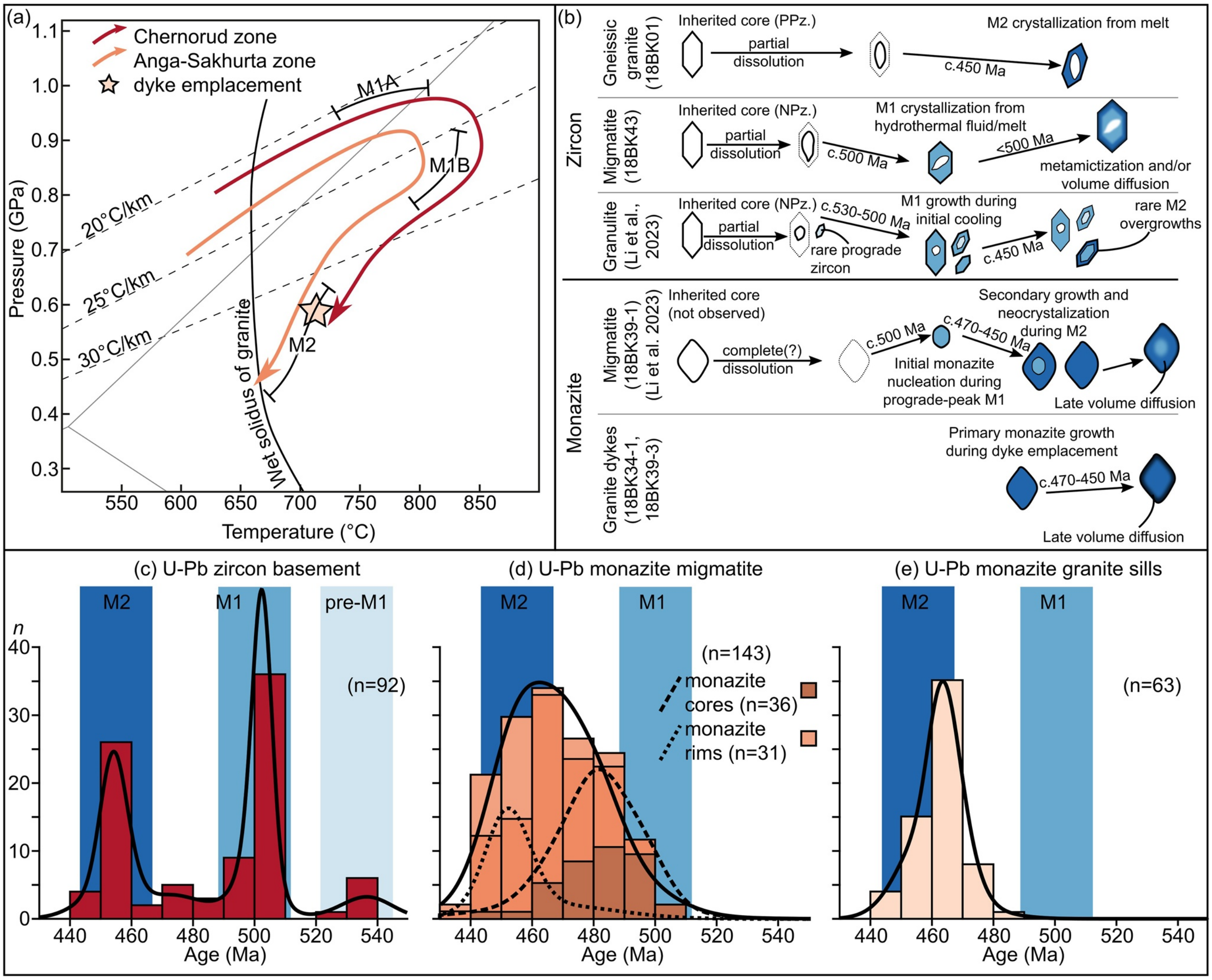

Figure 9. (a) Pressure-Temperature paths for the Chernorud Zone and Anga-Sakhurta Zone defined by Z. Y. Li et al. (2023). (b) Inferred sequence of zircon and monazite crystallization/dissolution in the studied samples from this study and Z. Y. Li et al. (2023). (c) U-Pb zircon ages from basement complexes in this study and Z. Y. Li et al. (2023). (d) U-Pb monazite ages from migmatite samples, this study and Z. Y. Li et al. (2023). (e) U-Pb monazite ages from granite sills presented in this study.

7.2. Geochronological Constraints of Partial Melting, Emplacement of Horizontal Granite Veins and Late Folding and Sinistral Wrenching

Geochronological studies carried-out on the Olkhon Terrane cover a large spectrum of metamorphic rocks, granitoids, and/or mafic/ultramafic rocks and result in a large number of isotopic ages ranging from the Precambrian to Early Devonian (Donskaya et al., 2017; Gladkochub et al., 2008b; Sklyarov et al., 2020b; Vladimirov et al., 2011; Volkova et al., 2010). Combined with new data from this study, their significances with respect to regional tectono-thermal evolution are discussed as follows.

7.2.1. Interpretation of U-Pb Zircon and Monazite Ages

In this study, Precambrian ages are recorded in zircon cores from nebulitic migmatite 18BK43-1 and gneissic granite 18BK01-1 samples (Figure 9b). For gneissic granite sample 18BK01, the calculated weighted mean age of 2,143 ± 24 Ma is obtained from oscillatory zoned zircon cores with Th/U ratios of 0.19–0.87, indicating igneous origin (Figure 6b) (Corfu et al., 2003). This age is older than the Paleoproterozoic basement known in the Zunduk Zone to the northern part of the Olkhon Terrane (Donskaya et al., 2017), but highlights an important inheritance from an ancient cratonic basement reported previously by a number of authors from similar rocks (e.g., Priyatkina et al., 2020; Turkina et al., 2010; Urmantseva et al., 2012). Neoproterozoic zircons, with a weighted mean age of 822 ± 7 Ma (Figure 6e), from the nebulitic migmatite sample 18BK43-1 have irregular, oscillatory, or sector zoning and Th/U ratios of 0.17–0.93 consistent with igneous origins (Corfu et al., 2003). This age is common in the CAOB basement (e.g., Kovach et al., 2013; Kuzmichev & Larionov, 2013; Z. X. Li et al., 2008) and similar ages have been reported from both the northern (Zunduk Zone) and southern (Orso Complex) parts of the Olkhon Terrane (Donskaya et al., 2017). Altogether, the inherited zircons indicate the presence of an old Paleoproterozoic and Neoproterozoic basement in the source region with possible Siberian and/or Mongolian basement affinity.

The next age cluster begins at c. 500 Ma. This age is recorded in zircon rims from the nebulitic migmatite sample 18BK43-1 and less commonly in monazite from migmatite 18BK39-1 (Figures 9c and 9d). In the anatectic migmatite sample from this study 18BK43-1, the analyzed zircons are dark and texture-less in CL images and Th/U ratios are low (0.04–0.28) consistent with typical metamorphic zircons (Harley et al., 2007). Moreover, high U and light-REE contents also indicate interaction with hydrothermal fluids and role for metamictization explaining the lack of a coherent population and high degree of discordance in the data from zircon rims (Figure 6f) (e.g., Hoskin, 2005). The oldest concordant ages (c. 495 Ma) may therefore be interpreted as onset of metamorphic crystallization given the regional context cited below. Monazites from migmatite sample 18BK39-1 yielded a spread of ages from 486 to 442 Ma where the ages from monazite cores are systematically older than those from rims (Figure 6k). The oldest monazite age from this sample is similar to the zircon ages from migmatite 18BK43-1. Indeed, the c. 500 Ma zircon and monazite age population is characteristic for an early stage of high-grade metamorphism and syn-kinematic granitoids in the Olkhon Terrane (Donskaya et al., 2017; Gladkochub et al., 2008a, 2008b; X. C. Li et al., 2009; Makrygina et al., 2014; Mikheev et al., 2017; Vladimirov et al., 2008, 2011). Similar ages were also identified in zircon from Chernorud Zone granulite and monazite from Anga-Sakhurta Zone migmatite and paragneiss in our previous study (Z. Y. Li et al., 2023). Accordingly, this age cluster can be considered as the timing of the early M1 metamorphism (Z. Y. Li et al., 2023) and relics of syn-orogenic magmatism and migmatization $D1_{MIG}$ (Mikheev et al., 2017).

The last group of zircon and monazite ages is ranging from c. 470 to 445 Ma and belongs to the most common age interval reported from numerous magmatic bodies in the Anga-Sakhurta Zone (Figures 9d and 9e) (Donskaya et al., 2013; Fedorovsky et al., 2010; Makrygina et al., 2014; Mikheev et al., 2017; Vladimirov et al., 2008). The studied granite vein samples 18BK34-1 and 18BK39-3 yielded monazite U-Pb age spread of 472–444 and 478–445 Ma, respectively (Figures 6h and 6n). Notably, in both samples the monazite grains exhibit clear core and rim textures in BSE images and rim analyses are systematically younger than their associated core analysis (Figures 6h and 6n). The monazite data from granite veins are comparable to the younger ages from migmatite 18BK39-1. This time frame is also bracketed by the youngest zircon age of gneissic granite 18BK01-1 (Figure 6b). In this sample, dark homogeneous CL zircon rims with Th/U ratios of 0.06–0.15, indicate a metamorphic origin (Corfu et al., 2003; Harley et al., 2007). It can be concluded that granite veins and gneissic granite recorded zircon and monazite U-Pb ages ranging from 470 to 445 Ma while the migmatite samples revealed presence of older c. 500 Ma zircons and monazites (Figures 9c and 9d). These younger ages were probably related to Ordovician remelting of the Cambrian orogenic edifice and intrusion of granite sills parallel to the primary Sh^1_{MIG} fabric. Altogether, the c. 445 Ma age can be considered as an upper limit of an important thermal event the duration of which is difficult to estimate. However, published zircon U-Pb data from various granitoids may suggest that the interval between 470 and 445 Ma is responsible for massive melting and intrusions of the main portions of granitoids in the Anga-Sakhurta Zone (Donskaya et al., 2013, 2017; Z. Y. Li et al., 2023; Mekhonoshin et al., 2013; Sklyarov et al., 2009, 2020b; Vladimirov et al., 2011).

The temporal relationships between Sh^1_{MIG} fabric and granite sills with horizontal sub-solidus to solid-state fabric are pivotal for D2 extensional hypothesis. In migmatite (samples 18BK43-1, 18BK39-1) zircons and monazites U-Pb ages ranging between 500 and 480 Ma were identified. However, granite show younger ages clustering around 470–445 Ma (Figures 6 and 9). The two age populations occur in a single subhorizontal fabric, which indicate that this structure recorded two important metamorphic and magmatic events. These relationships are best illustrated on large outcrop 18BK39 (Figure 10) in the western part of the Anga-Sakhurta Zone (Figure 2a). The key element of this 50–100 m long section are low strain domains preserving the original sub-horizontal fabric Sh^1_{MIG} and granite veins or sills that were emplaced parallel to the former fabric (Figure 10). Whereas the migmatite contains 500–480 Ma zircons, the veins do not contain them and instead show younger 470–445 Ma ages (Figure 9e). It can therefore be envisaged that the Sh^1_{MIG} developed during an early syn-collisional 500–480 Ma event as cited above and was re-used during a second 470–445 Ma event. Thus, the horizontal fabric in migmatite

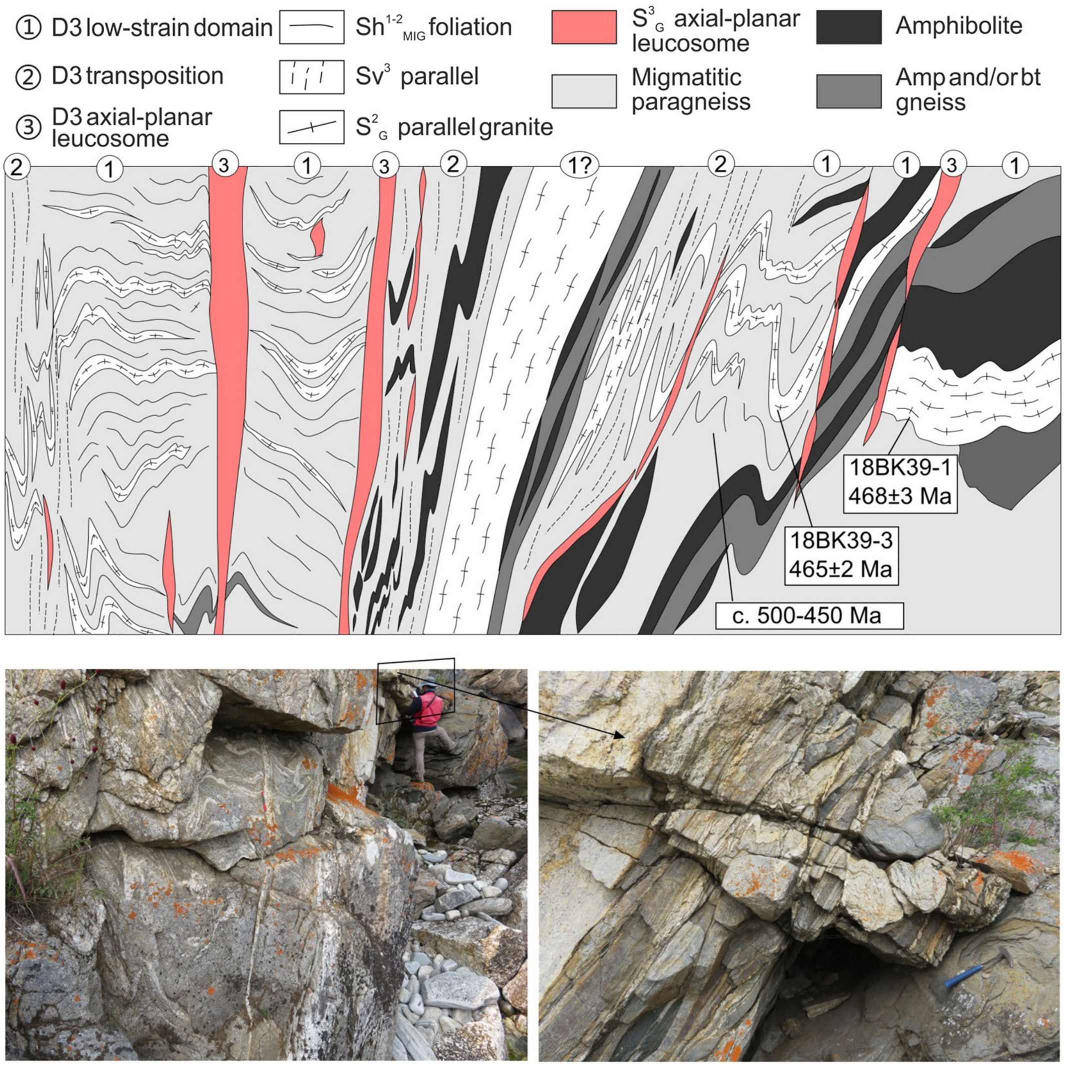

Figure 10. Idealized cross section across the c. 100 m long outcrop in the central part of the Anga-Sakhurta Zone (locality 18BK39). This outcrop shows sub-horizontal foliation Sh$^{1-2}_{MIG}$ in migmatitic paragneiss intruded by sub-horizontal leucosome sills with internal fabric S^2_G. The two fabrics are preserved in D3 low-strain domains and were togetherly folded by Fu^3 folds forming lithons that are surrounded by sub-vertical zones of D3 deformation. In these zones all Dh$^1_{MIG}$ and S^1_G fabrics are entirely transposed. The D3 zones and axial planes of Fu^3 folds are in places exploited by residual melts forming axial planar leucosomes indicating that the edifice was still hot and hence rheologically weak during D3.

is a composite structure which resulted from two events both associated with HT and melting; syn-collisional Cambrian lower crustal flow and thickening reaching 8 kbar at 770°C (M1) followed by mid-late Ordovician extension Eh$^2_{MIG}$ reaching ~4 kbar at 670°C (M2). The fabric in the migmatite should therefore be assigned as Sh$^{1-2}_{MIG}$ while fabric in granite sheets and sills as S^2_G (Figure 10). According to notation method of Beltrando et al. (2008) the early D1 and D2 deformation evolution of the Anga-Sakhurta Zone can be expressed as: Sh$^1_{MIG(530-500Ma)}$/Fr$^1_{MIG(530-500Ma)}$ => Eh$^2_{MIG(470-445Ma)}$ => Sh$^{1\text{-}2}_{MIG(470-445Ma)}$/S$^2_{G(470-445Ma)}$.

7.2.2. Interpretation of ^{40}Ar/^{39}Ar Biotite Ages

As stated above, the D3 is linked with upright folding of generally sub-horizontal or moderately dipping migmatite layering and magmatic fabrics (Figures 2e and 2f), which in some places underwent solid state recrystallization and deformation. Numerous observations indicate that this folding was associated with subsolidus post-anatectic deformation of granitic rocks and migmatite (Figures 3 and 5). Metamorphic studies of the Olkhon Terrane revealed that all tectonic zones went through amphibolite facies or higher-temperature metamorphism, and that the temperature was above 500ºC or high for M2 metamorphism (Z. Y. Li et al., 2023; Sklyarov et al., 2020a).

This temperature is far higher than the closure temperature of 320–290ºC for the biotite K-Ar system (Grove & Harrison, 1996; Harrison et al., 1985; Schaen et al., 2021). On the other hand, field and petrographic observations also indicate that the late sinistral shearing occurred at lower amphibolite to greenschist facies conditions as indicated by dynamic recrystallization of quartz and plagioclase and presence of muscovite in various mylonites (Figures 4f, 7d, and 7h).

As D3 affected the migmatite-magmatite terrane of the Anga-Sakhurta Zone after the last metamorphic crystallization at c.445 Ma, $^{40}Ar/^{39}Ar$ dating should indicate the age of post-D3 cooling of the Olkhon Terrane rocks and/or timing of the D3 shearing. The sample 18BK35-4 yielded an age of c.408 Ma and is characterized by Sh^{1}_{GRA} fabric folded by Fu^{3} fold (Figure 8a). The sample 18BK07-1 dated at ~421 Ma was taken at the contact zone between the Anga-Sakhurta Zone and medium grade Orso Complex dominated by Sv^{3} fabric (Figure 8g). In addition, two D3 mylonitic samples (18BK03-1 and 18BK53-2) yielded ages of c. 406 and c. 401 Ma, respectively (Figures 8c and 8e). The latter three samples are directly associated to D3 ductile shearing which operated at amphibolite facies to greenschist facies conditions (Figures 7d, 7f, and 7h). These ages may indicate a Devonian ~420–400 Ma interval of the activity of the D3 deformation. The sample 18BK35-4 affected only by Fu^{3} folding shows similar Devonian age implying that the cooling of the whole system through closure temperature ~320°–290°C (Grove & Harrison, 1996; Harrison et al., 1985; Schaen et al., 2021) was temporally related to D3. These ages can be compared to a number of biotite and muscovite $^{40}Ar/^{39}Ar$ data reported by Travin et al. (2009) and Vladimirov et al. (2011), pointing to a mean age of c. 415 Ma, which is interpreted as the timing of D3 shearing. However, there are a number of amphibole $^{40}Ar/^{39}Ar$ ages which reveal an average age of 435 Ma with a significant number of data clustering around 445 Ma from all tectonic zones. Travin et al. (2009) and Vladimirov et al. (2011) interpret these older ages as reflecting the timing of generalized lower amphibolite facies retrogression and cooling through the 500°C isotherm possibly associated with the onset of sinistral shearing. The Silurian onset of D3 and general cooling history of the Olkhon Terrane needs to be however confirmed by systematic petro-chronological analysis. Nevertheless, it can be concluded that the (Silurian?) Devonian (420–400 Ma) D3 deformation is an important event that resulted in two important structural elements observed in the Olkhon Terrane: (a) amphibolite to greenschist facies deformation at the contact with the Siberian block and (b) development of vertical sinistral shear zones and upright folding of sub-horizontal $Sh^{1-2}_{MIG(470-445Ma)}/S^{2}_{G(470-445Ma)}$ fabric in the migmatite of Anga-Sakhurta Zone.

Altogether, the deformation and thermal history of the Anga-Sakhurta Zone can be expressed using modified Beltrando et al. (2008) notation as follows: $Sh^{1}_{MIG(530-500Ma)}/Fr^{1}_{MIG(530-500Ma)}$ => $Eh^{2}_{MIG(470-445Ma)}$ => $Sh^{1-2}_{MIG(470-445Ma)}/S^{2}_{G(470-445Ma)}$, $Fu^{3}/Sv^{3}_{(435-400)}$ => $Ss^{3}_{amp\text{-}gre(420-400)}$.

7.3. Geodynamic Interpretation

New structural and geochronological data show that the Anga-Sakhurta Zone underwent a complex geodynamic evolution during the early Paleozoic times. There is a general consensus that the Anga-Sakhurta Zone is formed by a series of gneiss domes with migmatite-magmatite cores. This study shows that the migmatite in the cores of these domes preserve important records of Precambrian zircons implying that these rocks may be derived from re-melting of an old Siberian or CAOB type basement.

7.3.1. Migmatite-Magmatite Infrastructure and Growth of Core Complexes

The general structure of the Anga-Sakhurta Zone can be defined as HT migmatite-magmatite deep crust, which underlies the medium grade middle crust (Figure 2b). This structural edifice satisfies the definition of an orogenic infra- and superstructure as it was defined for instance in the Pyrenees (Zwart, 1986) and in many other orogens (e.g., Culshaw et al., 2006). In the Anga-Sakhurta Zone the infrastructure forms a large number of kilometer scale migmatite-magmatite domes visualized in schematic block diagram (Figure 11a) that are surrounded by medium-grade superstructure—that even in some cases reveals structural discordance with regards to the underlying migmatite and granitoids (Fedorovsky & Sklyarov, 2015). The medium-grade garnetiferous schist show metamorphic *P*–*T* conditions of 6–9 kbar at 600°C from the Orso complex of the Krestovaya Zone (Sklyarov et al., 2020a), which is compatible with preservation of early MP metamorphic gradient in the southernmost and lower grade part of the Olkhon system. This, together with preserved MP metamorphism in the Chernorud and Anga-Sakhurta zones indicate that the whole orogen suffered crustal thickening. In contrast, the infrastructure migmatite and paragneiss in the central part of the orogenic system (Anga-Sakhurta Zone) shows a pressure

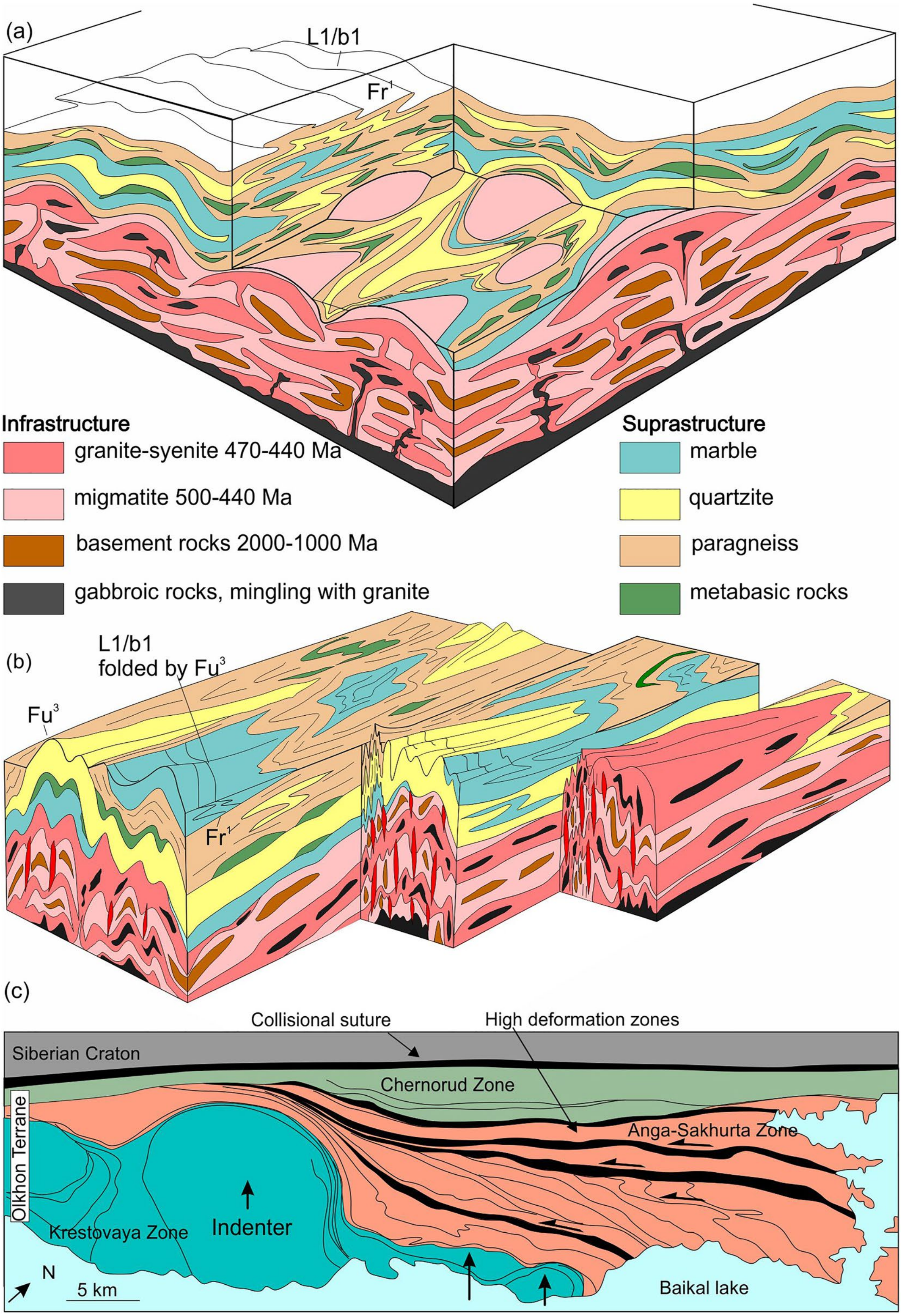

Figure 11.

and temperature drop to ~700°C and ~4 kbar with respect to initial conditions of 770°C and 8 kbar (Z. Y. Li et al., 2023). This metamorphic evolution, related to persistence of the sub-horizontal fabric at decreasing pressure, is compatible with important crustal thinning and crustal melting under extensional regime. The extensional event was probably also associated with an important elevation of mantle isotherms and partial melting of the mantle as indicated by massive emplacement of alkaline gabbro into granite magma chambers described by Sklyarov et al. (2001), Sklyarov and Fedorovsky (2006), and Fedorovsky et al. (2010). This extensional hot system possibly operated from 470 Ma and ended at around 445 Ma as indicated by several c. 445 Ma amphibole ^{40}Ar/^{39}Ar ages that are only slightly younger than this Late Ordovician thermal peak, indicating cooling of the whole edifice at that time.

7.3.2. Post-Extensional Shortening and Lateral Extrusion of the Anga-Sakhurta Zone

Most of the observed D3 folds reflect post-migmatitic and magmatic deformation events (e.g., Figures 3a, 3c, 3e, and 3g). However, in some cases there was observed massive transposition of earlier structures (e.g., Figures 4a, 5e, 5i, and 10) at upper amphibolite facies conditions or even associated with emplacement of axial planar residual melt (Figure 3f). All of which indicates that the massive shortening and exhumation of the Anga-Sakhurta Zone and the whole Olkhon Terrane in general started at amphibolite facies conditions and was finished by greenschist facies shearing and post-metamorphic folding. This NE-SW oriented upright folding leads to further amplification of semi-circular domes which became elliptical during their shortening with a long axis oriented at NE-SW direction. The shortening also resulted in pinching of rheologically weak superstructure between individual domes (Figure 11b). In the central part of the Anga-Sakhurta Zone the D3 deformation is responsible for massive transposition of all previously developed structures together with intrusion of axial planar leucosomes (residual melts) as it is exemplified by the large outcrop 18BK39 (Figure 10). Large scale folding of originally sub-horizontal or gently dipping fabric of the domes by upright folds was already described and illustrated by Fedorovsky (1997). However, it was not clear that the D3 deformation of infra- and super-structure was almost identical. With the new findings from this study, it can be concluded that the D3 shortening folded variably dipping but mostly sub-horizontal fabric of extensional domes of still hot crust and massively accentuated and shortened the supra-structural synforms. This deformation had to start after 445 Ma and affected the whole Olkhon Terrane thereafter.

This prominent shortening probably resulted in the formation of a steep "collisional suture zone" that reworked the granulite facies rocks of the Chernorud Zone at the boundary with the Siberian continent as discussed above (Figures 1 and 2a). In addition, this shortening event is related to northward progression of the whole Krestovaya Zone mafic promontory from SE to NW leading to the almost entire shortening of both the Chernorud and Anga-Sakhurta Zones (Figure 11c) (Fedorovsky & Sklyarov, 2015). However, before the arrival of the Birkhin indenter the whole orogenic zone suffered pure shear deformation—that is, D3 folding and shortening without massive lateral extrusion. Later, as the Birkhin promontory progressed, the whole system was extruded laterally to the NE and exploited previous pinched zones as sinistral shear zones at c. 420–400 Ma.

A model of sinistral shearing along the main northeast striking shear zones transecting the Olkhon Terrane was proposed by Fedorovsky and Sklyarov (2015), Fedorovsky et al. (2010, 2020) on the basis of large-scale drag folds and sigmoidal structures accompanying these zones. Their model is fully compatible with the slip-line model explaining left-lateral movements along west-northwest trending planes in SE Asia as a result of deformation of Asian crust related to northward movement of the Indian promontory (Molnar & Tapponnier, 1977; Tapponnier & Molnar, 1976). This feature was later successfully simulated using simple plasticine analog models of rigid block indentation and right-sided lateral extrusion (Tapponnier et al., 1982). We argue that the northwest-ward movement of Birkhin indentor, northeast-southwest orientation of principal shear zones and right-sided lateral extrusion of both the Chernorud and Anga-Sakhurta zones show similar kinematic features to the model explaining India-Asia convergence cited above. Even if micro-graphs (Figures 4c and 7d) show conflicting sense of shear, the general interpretation of sinistral translation along strike-slip zones imposed by northwestward moving block remains valid in the sense of the slip-line theory of Tapponnier and Molnar (1976). On top of that, the whole system suffered massive pure-shear shortening manifested by generalized Fu^3 folding or deformation pattern

Figure 11. (a) Conceptual 3D block diagram for the extensional doming phase within the Anga-Sakhurta Zone of the Olkhon Terrane. This panel shows formation of migmatite-magmatite domes intruded by alkaline gabbro during generalized extension and rise of partially molten lower crust. The stronger superstructure accommodates general stretching of the crust. (b) Conceptual section through the Anga-Sakhurta Zone following D3 shortening and strike-slip faulting. This panel shows amplification of extensional domes, their partial reworking during D3 and intrusion of vertical axial planar veins filled by residual melts. Highly anisotropic superstructure suffered massive shortening and development of pinched synforms exploited by sinistral shear zones. Note that the displacement of blocks does not reflect real kinematics, but it serves to better appreciate general architecture of orogeny after shortening and shearing. (c) Tectonic map of the Olkhon Terrane modified after Fedorovsky and Sklyarov (2015) showing lateral extrusion of the Anga-Sakhurta Zone along large scale D3 shear zones exploiting both pinched synforms and limits of main tectonic zones constituting the Olkhon Terrane.

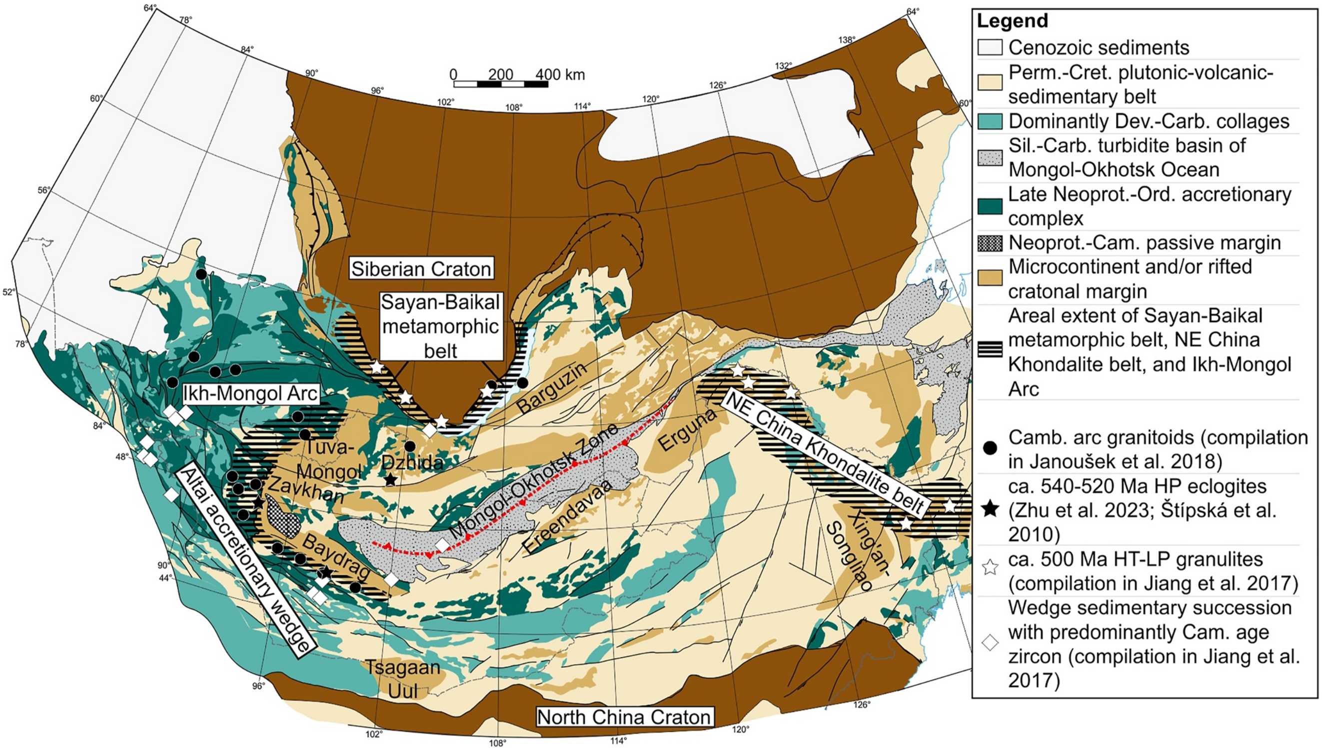

Figure 12. Simplified tectonic map of the eastern Central Asian Orogenic Belt after Y. D. Jiang et al. (2017) showing spatial distribution of major superterranes and distribution of magmatic, metamorphic, and sedimentary sequences associated to Cambro-Ordovician accretion/collision in the Mongolian Collage.

along the steep "collisional suture zone" of Fedorovsky et al. (2020) at the margin of the Siberian Craton. Generalized, possibly partitioned, pure-shear dominated transpression superposed on rotating high-strain (fault) zones is a potential mechanism explaining the lack of unambiguous kinematic indicators or their obliteration during progressively increasing pure-shear component (e.g., Jezek et al., 2002; Schulmann et al., 2003).

7.4. Implications for Early Accretionary Evolution of the CAOB

Early Cambrian collisional, Ordovician extensional and Silurian-Devonian compressional cycles depicted in the Olkhon Terrane in this work can be compared to sequences of tectonic events described along the Siberian margin. In particular, Delvaux et al. (1995) on the basis of fault analysis, reports a late Cambrian-early Ordovician N-S compression followed by late Silurian-Early Devonian NW-SE compression which corroborates our findings. Similarly, de Boisgrollier et al. (2009) studied deformation of the Siberian platform along the Patom range and reported first late Proterozoic and second Devonian collisional stages and an important Ordovician extensional stage broadly confirming the model presented here. This study also allows comparison of its tectonic evolution with different sectors of the Mongolian Collage, which are marked by the development of an early Paleozoic subduction-accretion complex riming the margins of Precambrian microcontinents (Figure 12). Numerous early Paleozoic U-Pb zircon ages have been reported from the Precambrian microcontinents distributed in the eastern segment of the CAOB in the NE China, including c. 495 Ma in the Erguna Block, c. 494 Ma in the Xing'an Block, c. 502 Ma in the Jiamusi and Khanka Block (Zhou & Wilde, 2013; Zhou et al., 2011a, 2011b, 2018). These data were interpreted to reflect the existence of a c. 1,300 km long c. 500 Ma metamorphic belt called the "NE China Khondalite Belt" (Figure 12) (Zhou et al., 2018). There, the examined rocks were mostly hornblende-plagioclase and garnet-sillimanite-K-feldspar gneiss indicative for upper amphibolite to granulite facies conditions. Paragneiss from the Mashan Complex of the Jiamusi Block was characterized by a clockwise P–T path with granulite-facies peak metamorphic conditions of approximately 850°C and 7.4 kbar (J. Jiang, 1992) and amphibolite-facies retrograde conditions of 500°–550°C at 6–7 kbar (Cao et al., 1992). Cambrian metamorphism was also reported from the central segment of the Mongolian Collage represented by those recorded in the Zavkhan, Baydrag and the Tuva-Mongol microcontinents in Mongolia (e.g., Kozakov et al., 2008; Štípská et al., 2010; Zhu et al., 2023). In these regions two principle metamorphic phases were recognized: (a) A HP Early Cambrian (c. 540–520 Ma) phase and (b) a Late Cambrian–Early Ordovician (500–470 Ma) HT phase (Kozakov et al., 2015). The early metamorphic phase is characterized by the presence of kyanite-garnet bearing paragneiss with peak conditions of 750°C at 9–10 kbar in the Tuva-Mongol block constrained at c. 536 Ma (Kozakov et al., 2019). In addition, rare eclogite occurrences have been documented from the southern margin of the Baydrag microcontinent (Buriánek et al., 2017), the western margin of the Zavkhan microcontinent and the southern margin of the Dzhida Arc (Zhu et al., 2023). Štípská et al. (2010) presented a c. 540 Ma muscovite ^{40}Ar/^{39}Ar age from the eclogitized wedge thrust over the Baydrag block and Zhu et al. (2023) reported c. 520 Ma zircon U-Pb ages from the eclogitized wedges thrust over the Zavkhan (Urgamal) and Tabarbagatay (Tsengel) blocks, collectively attesting to the presence of an Early Cambrian HP metamorphic phase in the region. The later HT-LP metamorphic phase developed in the Tuva-Mongol and Zavkhan microcontinents and is represented by garnet-cordierite-sillimanite bearing migmatite with *P–T* conditions of 620°–670°C and 4–4.6 kbar (Kozakov et al., 2019). This phase is coeval with extensive granitoid magmatism affecting the southern and western margins of the Mongolian microcontinents, which constitutes a part of the 1,800 km long Ikh-Mongol Arc (Janoušek et al., 2018). Back to the southern Siberia, the c. 500 Ma Sayan-Baikal collisional belt is composed of several metamorphic complexes (Figure 12) (Derba c. 498, Kitoikin c. 473, Sludynaka c. 488, and Olkhon c. 498 Ma, Donskaya et al., 2000). Because of similarities in both metamorphic conditions and peak metamorphic ages between the Sayan-Baikal collisional belt and the NE China Khondalite Belt, Zhou et al. (2011a, 2011b) proposed that both orogenic systems were mutually connected and formed a continuous orogenic system flanking the whole SE margin of the Siberian Craton during Late Cambrian times.

Despite the above mentioned similarities, there are also significant differences which contest a simple correlation between these orogenic belts. Available geochronological and metamorphic data indicated that the NE China Khondalite Belt recorded only one c. 500 Ma HT peak. This together with coeval metamorphic event recorded in the Sayan-Baikal collisional belt (Donskaya et al., 2000; Gladkochub et al., 2008b; Nozhkin et al., 2005; Salnikova et al., 1998), led Wilde (2015) to propose a direct correlation of the Sayan-Baikal belt and Khondalite belt at around 500 Ma and suggested the existence of a continuous granulite facies collisional belt along the whole southern Siberian margin. According to Zhou and Wilde (2013) the originally peri-Siberian Kondalite belt was separated from its this position by opening of the Mongol-Okhotsk Ocean in Silurian times. It is evident that the Olkhon Terrane, which is the best studied segment of the Sayan-Baikal collisional belt, shows significantly more complex tectonic evolution compared to NE China Khondalite Belt where Ordovician 470–445 Ma extensional, Silurian-Devonian 435–400 Ma collisional and wrenching events are missing or so far not described. On the other hand, the central segment of the Mongolian tract of the CAOB shows tectonic evolution that can be compared to that proposed for the Olkhon Terrane. There, the Cambrian HP metamorphism affecting the western margin of Tuva-Mongolian continent and southern margin of the Baydrag continent (Kozakov et al., 2019; Štípská et al., 2010; Zhu et al., 2023) matches well with the onset of HP metamorphism at the Chernorud Zone of the Olkhon Terrane (Gladkochub et al., 2008b; X. C. Li et al., 2009; Z. Y. Li et al., 2023; Makrygina & Petrova, 1998). This suggests almost coeval syn-collisional metamorphism in the northern and central segment of the Mongolian Collage. The collisional event culminated at c.500 Ma in the Olkhon Terrane, which is possibly reflected by the HT metamorphic event coeval with the Andean type arc magmatism affecting both central and eastern segments of the Mongolian Collage (e.g., Janoušek et al., 2018; Kozakov et al., 2012; Zhou et al., 2018).

The question arises as what are the equivalents of the 470–445 Ma HT extensional event and subsequent 435–400 Ma shortening affecting the Anga-Sakhurta Zone in the central segment of the Mongolian Collage. This period of evolution is characterized by development of a giant volcano-sedimentary wedge in the Mongolian Altai (Xiao et al., 2009), which reflects continuous supplies of detritus from the Ikh-Mongol Arc and Precambrian crust of the Mongolian Zavkhan and Baydrag blocks during roll-back of the Paleo-Pacific oceanic plate (Y. D. Jiang et al., 2017). Given that the presence of paragneiss with back-arc geochemical signatures and the emplacement of 470–450 Ma alkaline gabbro in the Anga-Sakhurta Zone, it therefore can be assumed that the extensional event, marked by HT metamorphism and extensional doming in the Anga-Sakhurta Zone, developed at the back-arc setting in the Olkhon Terrane while fore-arc sedimentation and volcanism operated in the Mongolian Altai (Buriánek et al., 2022; Sukhbaatar et al., 2022). Soejono et al. (2021) further showed that the Ordovician sedimentary wedge of the Mongolian Altai was affected by Late Ordovician–Early Silurian (c. 440–430) prograde metamorphism associated with crustal thickening. This metamorphic event was associated with the development of a vertical metamorphic fabric resulting from massive horizontal shortening. We argue that this shortening in the central segment of the

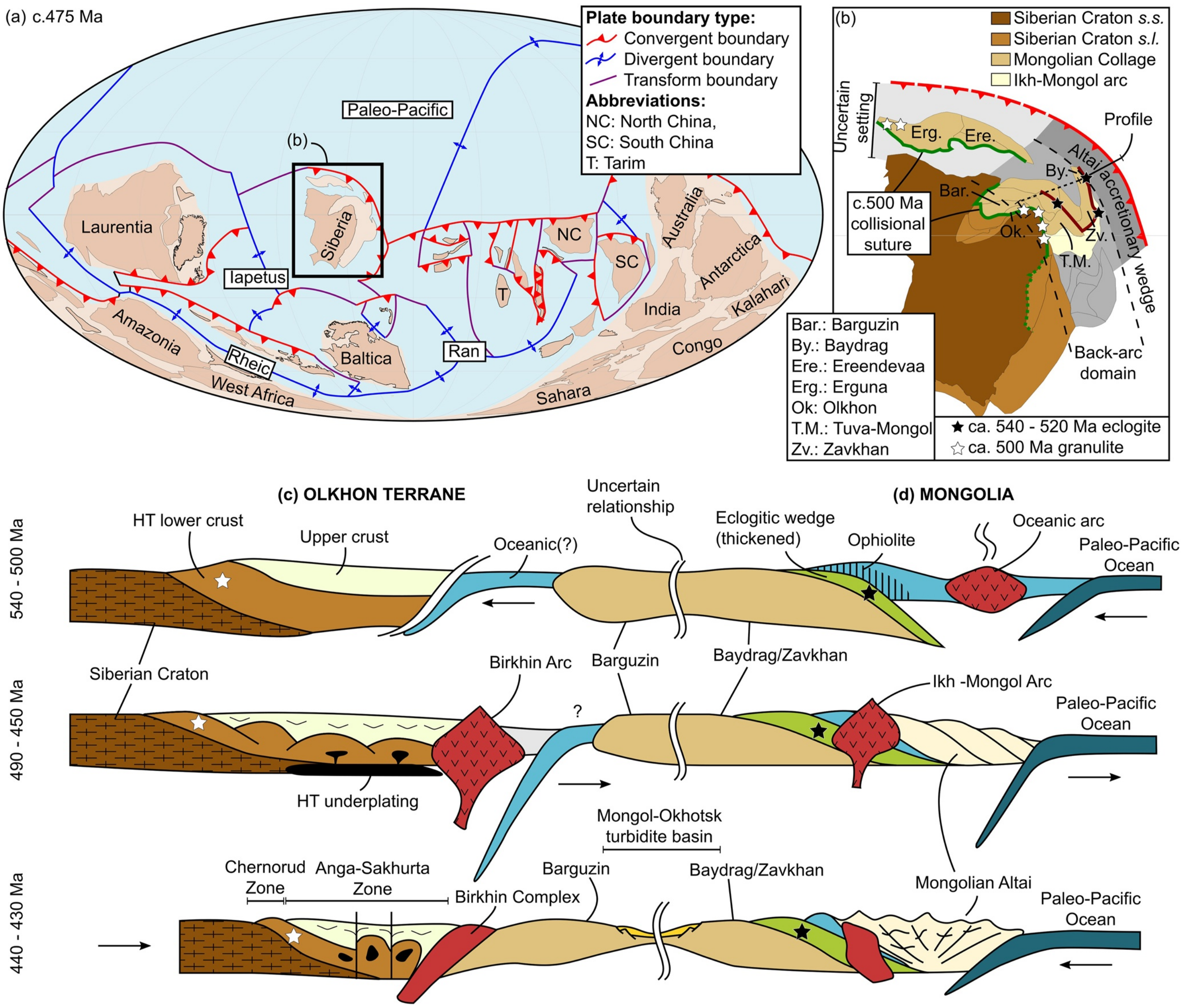

Figure 13. (a) Plate tectonic reconstruction for the Early Ordovician (c. 475 Ma) after Merdith et al. (2021). (b) Close-up view of Siberian Craton and Mongolian Collage terranes depicting interpreted geodynamic scenario following c. 500 Ma collision orogenic event and at onset of c. 470–445 Ma extensional event. Definitions of Siberia sensu stricto and Siberia sensu lato after Cocks and Torsvik (2007). (c, d) 2-D geodynamic profiles depicting the proposed evolution of the (c) Olkhon Terrane and (d) Mongolian sections. Note in the second panel that both the Birkhin and Ikh Mongol arc systems are depicted as still active at c. 490 Ma (e.g., Donskaya et al., 2017; Janoušek et al., 2018) but would shortly thereafter cease, while sedimentary accretion in the Altai accretionary wedge continues to the Late Ordovician (e.g., Y. D. Jiang et al., 2017). The approximate location of each profile is depicted in panel (b).

Mongolian Collage temporally corresponds to the D3 upright folding related to shortening in the Olkhon Terrane. Finally, the Devonian sinistral shearing reported from the Olkhon Terrane can be at least temporally correlated with upright folding and doming recently reported from the Chinese Altai (Kong et al., 2022; Wang et al., 2021). However, the kinematic correlation of the Olkhon Terrane and Chinese Altai is so far not possible.

Taken together, the Olkhon Terrane and the central segment of the Mongolian Collage show a nearly coeval sequence of contractional and extensional events. However, the tectonic environment was different. In the north, the Early Cambrian is characterized by hot arc-continent collision (Donskaya et al., 2000, 2017; Z. Y. Li et al., 2023), whereas the south is characterized by thrusting of eclogite-bearing accretionary wedge (Štípská et al., 2010), moderate crustal thickening (Kozakov et al., 2019) and emplacement of late Proterozoic ophiolite sequences onto the continent (Figure 13) (Buriánek et al., 2017). Subsequent back-arc extension related HT metamorphic and magmatic event in the north correlates with massive sediment deposition in the fore-arc basin in the south (Figure 13) (Buriánek et al., 2022). This event probably reflects that the whole peri-Siberian system was subjected to large-scale rollback of paleo-Pacific oceanic plate which induced stretching of the overriding supra-subduction system (e.g., Y. D. Jiang et al., 2017). The switch to Early Silurian compression can be interpreted in terms of renewed advancing mode of the subducting plate and generalized shortening of the whole peri-Siberian realm (Figure 13). The tectonic switches reported in the northern and central segments of the Mongolian Collage were not so far reported from the NE China Khondalite Belt where detailed structural and coupled metamorphic petrology studies are missing.

Finally, the dimension of proposed peri-Siberian Mongolian collage (Wilhem et al., 2012; Xiao et al., 2015) is similar to the modern SE Asia archipelago (Wakita et al., 2013) or to pene-contemporaneous Delamerian-Lachlan system of eastern Australia (Foden et al., 2006; Foster & Gray, 2000). The mechanism of progressive collision of microblocks previously detached from the continental mainland above the controlling subduction of a peripheral oceanic domain closely resembles SE Asia models proposed by Wakita et al. (2013) and Pubellier and Meresse (2013). On the other hand, the time-scales of compression-extension-compression cycle mimics the similar peri-Pacific cycle of the Tasmanides as demonstrated by Gray and Foster (2004). Altogether, the Mongolian collage may represent a world-class laboratory, where length- and time-scales of contrasting collisional processes on the continental side of Siberia and subduction-accretionary processes along subducting peripheral Paleo-Pacific Ocean can be studied and understood.

8. Conclusions

New structural, petrographic, zircon/monazite U–Pb and biotite $^{40}Ar/^{39}Ar$ age data from the Anga-Sakhurta Zone of the Olkhon Terrane allow clarifying the early Paleozoic tectono-thermal history and interactions between peri-Siberian orogenic system and Siberian Craton. The principal conclusions are as follows.

1. The Olkhon Terrane underwent moderate Cambrian crustal thickening and formation of horizontal HT fabric in response to the collision between the Siberian Craton and peri-Siberian orogenic system. This early fabric was affected by mid-late Ordovician crustal extension in association with development of migmatite-magmatite domes and emplacement of partial melts (c. 470–445 Ma granite sills) parallel to the sub-horizontal mechanical anisotropy.
2. Subsequent Silurian shortening led to amplification of the domal structures, upright folding and heterogeneous vertical transposition of the composite horizontal fabric.
3. Ultimate north-westward indentation of the Birkhin Complex promontory into progressively cooled crust of the Anga-Sakhurta Zone caused lateral extrusion and sinistral shearing in the region. Strong localization of deformation was related to exhumation and cooling of the entire crustal section.
4. Early Paleozoic tectonic switches revealed in the Olkhon Terrane can be correlated with NE China Khondalite Belt and the central segment of the Mongolian Collage advocating their coherent supra-subduction evolution.

Data Availability Statement

The geochronological data used in this paper are available in Tables S1 and S2 and Figure S1, which are available in the Mendeley Data Repository (https://doi.org/10.17632/jvpbh5bygv.2) (Li & Jiang, 2023).

Acknowledgments
This work was supported by the National Natural Science Foundation of China (42022017, 42372240, and 42021002), the International Partnership Program of Chinese Academy of Sciences (132744KYSB20190039), and by the Czech Science Foundation (Grant 19-27682X). The fieldwork was done on the state assignment of IGM SB RAS with the financial support of the Ministry of Science and Higher Education of the Russian Federation. We wish to also thank Tan Shu and Ya-Zhou Miao for their help during the experimental analysis. We are indebted to the editor, reviewer WJ Collins and an anonymous reviewer for the constructive reviews and valuable comments that improved the manuscript.

References

Aleinikoff, J. N., Schenck, W. S., Plank, M. O., Srogi, L., Fanning, C. M., Kamo, S. L., & Bosbyshell, H. (2006). Deciphering igneous and metamorphic events in high-grade rocks of the Wilmington Complex, Delaware: Morphology, cathodoluminescence and backscattered electron zoning, and SHRIMP U-Pb geochronology of zircon and monazite. *Geological Society of America Bulletin*, *118*(1–2), 39–64. https://doi.org/10.1130/b25659.1

Améglio, L., Vigneresse, J. L., & Bouchez, J. L. (1997). Granite pluton geometry and emplacement mode inferred from combined fabric and gravity data. *Granite: From segregation of melt to emplacement fabrics*, 199–214.

Bachmann, O., Schoene, B., Schnyder, C., & Spikings, R. (2010). The $^{40}Ar/^{39}Ar$ and U/Pb dating of young rhyolites in the Kos-Nisyros volcanic complex, Eastern Aegean Arc, Greece: Age discordance due to excess ^{40}Ar in biotite. *Geochemistry, Geophysics, Geosystems*, *11*(8), Q0AA08. https://doi.org/10.1029/2010gc003073

Bai, X. J., Qiu, H. N., Liu, W. G., & Mei, L. F. (2018). Automatic $^{40}Ar/^{39}Ar$ dating techniques using multicollector ARGUS VI noble gas mass spectrometer with self-made peripheral apparatus. *Journal of Earth Sciences*, *29*(2), 408–415. https://doi.org/10.1007/s12583-017-0948-9

Beaumont, C., Nguyen, M., Jamieson, R. A., & Ellis, S. (2006). *Crustal flow modes in large hot orogens* (Vol. 268, p. 91). Special Publication-Geological Society of London.

Beltrando, M., Lister, G., Hermann, J., Forster, M., & Compagnoni, R. (2008). Deformation mode switches in the Penninic units of the Urtier valley (western Alps): Evidence for a dynamic orogen. *Journal of Structural Geology*, *30*(2), 194–219. https://doi.org/10.1016/j.jsg.2007.10.008

Buriánek, D., Schulmann, K., Hrdličková, K., Hanžl, P., Janoušek, V., Gerdes, A., & Lexa, O. (2017). Geochemical and geochronological constraints on distinct Early-Neoproterozoic and Cambrian accretionary events along southern margin of the Baydrag Continent in western Mongolia. *Gondwana Research*, *47*, 200–227. https://doi.org/10.1016/j.gr.2016.09.008

Buriánek, D., Soejono, I., Schulmann, K., Janoušek, V., Hanžl, P., Čáp, P., et al. (2022). Subduction-controlled temporal and spatial variations in early Palaeozoic sedimentary and volcanic record of the Mongol-Altai Domain. *Journal of Asian Earth Sciences*, *230*, 105182. https://doi.org/10.1016/j.jseaes.2022.105182

Cao, X., Dang, Z. X., Zhang, X., Jiang, J., & Wang, H. (1992). *Jiamusi composite terranes* (Vol. 19, p. 224). Jilin Publishing House of Science and Technology.

Clay, P. L., Kelley, S. P., Sherlock, S. C., & Barry, T. L. (2011). Partitioning of excess argon between alkali feldspars and glass in a young volcanic system. *Chemical Geology*, *289*(1–2), 12–30. https://doi.org/10.1016/j.chemgeo.2011.07.005

Cocks, L. R. M., & Torsvik, T. H. (2007). Siberia, the wandering northern terrane, and its changing geography through the Palaeozoic. *Earth-Science Reviews*, *82*(1–2), 29–74. https://doi.org/10.1016/j.earscirev.2007.02.001

Corfu, F., Hanchar, J. M., Hoskin, P. W., & Kinny, P. (2003). Atlas of zircon textures. *Reviews in Mineralogy and Geochemistry*, *53*(1), 469–500. https://doi.org/10.2113/0530469

Cosgrove, J. (1997). The influence of mechanical anisotropy on the behaviour of the lower crust. *Tectonophysics*, *280*(1–2), 1–14. https://doi.org/10.1016/s0040-1951(97)00145-5

Culshaw, N., Beaumont, C., & Jamieson, R. A. (2006). The orogenic superstructure-infrastructure concept: Revisited, quantified, and revived. *Geology*, *34*(9), 733–736. https://doi.org/10.1130/g22793.1

de Boisgrollier, T., Petit, C., Fournier, M., Leturmy, P., Ringenbach, J. C., San'kov, V. A., et al. (2009). Palaeozoic orogeneses around the Siberian craton: Structure and evolution of the Patom belt and foredeep. *Tectonics*, *28*(1), TC1005. https://doi.org/10.1029/2007tc002210

Delvaux, D., Moeys, R., Stapel, G., Melnikov, A., & Ermikov, V. (1995). Palaeostress reconstructions and geodynamics of the Baikal region, Central Asia, Part I. Palaeozoic and Mesozoic pre-rift evolution. *Tectonophysics*, *252*(1–4), 61–101. https://doi.org/10.1016/0040-1951(95)00090-9

Dobrzhinetskaya, L., Molchanova, T., Sonyushkin, V., Likhachev, A., & Fedorovsky, V. (1992). Thrust and shear plastic deformation in the metamorphic complex of Olkhon region (Western Pribaikalia). *Geotektonika*, (2), 58–71.

Donskaya, T. V., Gladkochub, D. P., Fedorovsky, V. S., Mazukabzov, A. M., Cho, M., Cheong, W., & Kim, J. (2013). Synmetamorphic granitoids (~490 Ma) as accretion indicators in the evolution of the Ol'khon terrane (western Cisbaikalia). *Russian Geology and Geophysics*, *54*(10), 1205–1218. https://doi.org/10.1016/j.rgg.2013.09.006

Donskaya, T. V., Gladkochub, D. P., Fedorovsky, V. S., Sklyarov, E. V., Cho, M., Sergeev, S. A., et al. (2017). Pre-collisional (>0.5 Ga) complexes of the Olkhon terrane (southern Siberia) as an echo of events in the Central Asian Orogenic belt. *Gondwana Research*, *42*, 243–263. https://doi.org/10.1016/j.gr.2016.10.016

Donskaya, T. V., Sklyarov, E. V., Gladkochub, D. P., Mazukabzov, A. M., Sal'nikova, E. B., Kovach, V. P., et al. (2000). The Baikal collisional metamorphic belt. *Doklady Earth Sciences*, *374*(7), 1075–1079.

Faure, M., & Pons, J. (1991). Crustal thinning recorded by the shape of the Namurian-Westphalian leucogranite in the Variscan belt of the northwest Massif Central, France. *Geology*, *19*(7), 730–733. https://doi.org/10.1130/0091-7613(1991)019<0730:ctrbts>2.3.co;2

Fedorovsky, V. S. (1997). Dome tectonics in the Caledonian collision system of western Cisbaikalia. *Geotectonics*, *31*(6), 483–497.

Fedorovsky, V. S., Donskaya, T. V., Gladkochub, D. P., Khromykh, S. V., Mazukabzov, A. M., Mekhonoshin, A. S., et al. (2005). The Ol'khon collision system (Baikal region).

Fedorovsky, V. S., & Sklyarov, E. V. (2015). The Olkhon geodynamic proving ground (lake Baikal): High resolution satellite data and geological maps of new generation. *Geodynamics & Tectonophysics*, *1*(4), 331–418. https://doi.org/10.5800/GT-2010-1-4-0026

Fedorovsky, V. S., Sklyarov, E. V., Gladkochub, D. P., Mazukabzov, A. M., Donskaya, T. V., Lavrenchuk, A. V., et al. (2020). Collision system of west Pribaikalie: Aerospace geological map of Olkhon region (Baikal, Russia). *Geodynamics & Tectonophysics*, *11*(3), 447–452. https://doi.org/10.5800/gt-2020-11-3-0485

Fedorovsky, V. S., Sklyarov, E. V., Izokh, A. E., Kotov, A. B., Lavrenchuk, A. V., & Mazukabzov, A. M. (2010). Strike-slip tectonics and subalkaline mafic magmatism in the Early Paleozoic collisional system of the western Baikal region. *Russian Geology and Geophysics*, *51*(5), 534–547. https://doi.org/10.1016/j.rgg.2010.04.009

Foden, J., Elburg, M. A., Dougherty-Page, J., & Burtt, A. (2006). The timing and duration of the Delamerian Orogeny: Correlation with the Ross Orogen and implications for Gondwana assembly. *The Journal of Geology*, *114*(2), 189–210. https://doi.org/10.1086/499570

Foster, D. A., & Gray, D. R. (2000). Evolution and structure of the Lachlan fold belt (Orogen) of eastern Australia. *Annual Review of Earth and Planetary Sciences*, *28*(1), 47–80. https://doi.org/10.1146/annurev.earth.28.1.47

Gladkochub, D. P., Donskaya, T. V., Fedorovskii, V. S., Mazukabzov, A. M., Sklyarov, E. V., Lavrenchuk, A. V., & Lepekhina, E. N. (2014). Fragment of the early Paleozoic (~500 Ma) island arc in the structure of the Olkhon terrane, Central Asian fold belt. *Doklady Earth Sciences*, *457*(2), 905–909. https://doi.org/10.1134/s1028334x14080042

Gladkochub, D. P., Donskaya, T. V., Fedorovsky, V. S., Mazukabzov, A. M., Larionov, A. N., & Sergeev, S. A. (2010a). The Olkhon metamorphic terrane in the Baikal region: An Early Paleozoic collage of Neoproterozoic active margin fragments. *Russian Geology and Geophysics*, *51*(5), 447–460. https://doi.org/10.1016/j.rgg.2010.04.001

Gladkochub, D. P., Donskaya, T. V., Fedorovsky, V. S., Mazukabzov, A. M., Wingate, M. T. D., Poller, U., & Todt, W. (2008a). New data on the age and protolith of granulites of the Olkhon collisional system (Baikal Region). *Doklady Earth Sciences*, *419*(2), 417–422. https://doi.org/10.1134/s1028334x08030148

Gladkochub, D. P., Donskaya, T. V., Ivanov, A. V., Ernst, R., Mazukabzov, A. M., Pisarevsky, S. A., & Ukhova, N. (2010b). Phanerozoic mafic magmatism in the southern Siberian craton: Geodynamic implications. *Russian Geology and Geophysics*, *51*(9), 952–964. https://doi.org/10.1016/j.rgg.2010.08.005

Gladkochub, D. P., Donskaya, T. V., Sklyarov, E. V., Fedorovsky, V. S., Mazukabzov, A. M., Stanevich, A. M., et al. (2017). In D. P. Gladkochub & T. V. Donskaya (Eds.), *The anatomy of the olkhon terrane: Cross section from the southern margin of the siberian craton into the northern Central Asian Orogenic Belt*. The Institute of the Earth's Crust of SB RAS.

Gladkochub, D. P., Donskaya, T. V., Wingate, M. T. D., Poller, U., Kroner, A., Fedorovsky, V. S., et al. (2008b). Petrology, geochronology, and tectonic implications of c. 500 Ma metamorphic and igneous rocks along the northern margin of the Central Asian Orogen (Olkhon terrane, Lake Baikal, Siberia). *Journal of the Geological Society*, *165*(1), 235–246. https://doi.org/10.1144/0016-76492006-125

Gladkochub, D. P., Nicoll, G., Stanevich, A. M., Mazukabzov, A. M., Sklyarov, E. V., Pisarevsky, S. A., et al. (2013). Age and sources of late precambrian sedimentary sequences of the Southern Baikal Region: Results of the U-Pb LA-ICP-MS dating of detrital zircons. *Doklady Earth Sciences*, *450*(1), 494–498. https://doi.org/10.1134/s1028334x13050097

Gordienko, I. V., Filimonov, A. V., Minina, O. R., Gornova, M. A., Medvedev, A. Y., Klimuk, V. S., et al. (2007). Dzhida island-arc system in the Paleoasian Ocean: Structure and main stages of Vendian-Paleozoic geodynamic evolution. *Russian Geology and Geophysics*, *48*(1), 91–106. https://doi.org/10.1016/j.rgg.2006.12.009

Gray, D., & Foster, D. (2004). Tectonic evolution of the Lachlan Orogen, southeast Australia: Historical review, data synthesis and modern perspectives. *Australian Journal of Earth Sciences*, *51*(6), 773–817. https://doi.org/10.1111/j.1400-0952.2004.01092.x

Grove, M., & Harrison, T. M. (1996). ^{40}Ar* diffusion in Fe-rich biotite. *American Mineralogist*, *81*(7–8), 940–951. https://doi.org/10.2138/am-1996-7-816

Harley, S. L., Kelly, N. M., & Möller, A. (2007). Zircon behaviour and the thermal histories of mountain chains. *Elements*, *3*(1), 25–30. https://doi.org/10.2113/gselements.3.1.25

Harrison, T. M., Duncan, I., & Mcdougall, I. (1985). Diffusion of ^{40}Ar in biotite: Temperature, pressure and compositional effects. *Geochimica et Cosmochimica Acta*, *49*(11), 2461–2468. https://doi.org/10.1016/0016-7037(85)90246-7

Hénocque, O., Ruffet, G., Colin, F., & Féraud, G. (1998). ^{40}Ar/^{39}Ar dating of West African lateritic cryptomelanes. *Geochimica et Cosmochimica Acta*, *62*(16), 2739–2756. https://doi.org/10.1016/s0016-7037(98)00185-9

Hoskin, P. W. O. (2005). Trace-element composition of hydrothermal zircon and the alteration of Hadean zircon from the Jack Hills, Australia. *Geochimica et Cosmochimica Acta*, *69*(3), 637–648. https://doi.org/10.1016/j.gca.2004.07.006

Jackson, S. E., Pearson, N. J., Griffin, W. L., & Belousova, E. A. (2004). The application of laser ablation-inductively coupled plasma-mass spectrometry to in situ U–Pb zircon geochronology. *Chemical Geology*, *211*(1–2), 47–69. https://doi.org/10.1016/j.chemgeo.2004.06.017

Jamieson, R. A., & Beaumont, C. (2013). On the origin of orogens. *Bulletin*, *125*(11–12), 1671–1702. https://doi.org/10.1130/b30855.1

Jamieson, R. A., Beaumont, C., Nguyen, M., & Lee, B. (2002). Interaction of metamorphism, deformation and exhumation in large convergent orogens. *Journal of Metamorphic Geology*, *20*(1), 9–24. https://doi.org/10.1046/j.0263-4929.2001.00357.x

Janoušek, V., Jiang, Y. D., Buriánek, D., Schulmann, K., Hanžl, P., Soejono, I., et al. (2018). Cambrian–Ordovician magmatism of the Ikh-Mongol Arc system exemplified by the Khantaishir magmatic complex (lake zone, south–central Mongolia). *Gondwana Research*, *54*, 122–149. https://doi.org/10.1016/j.gr.2017.10.003

Jeřábek, P., Lexa, O., Schulmann, K., & Plašienka, D. (2012). Inverse ductile thinning via lower crustal flow and fold-induced doming in the West Carpathian Eo-Alpine collisional wedge. *Tectonics*, *31*(5), TC5002. https://doi.org/10.1029/2012tc003097

Jezek, J., Schulmann, K., & Thompson, A. (2002). Strain partitioning in front of an obliquely convergent indenter. *EGU Stephan Mueller Special Publ Ser*, *1*, 93–104. https://doi.org/10.5194/smsps-1-93-2002

Jiang, J. (1992). Peak regional metamorphism of the khondalite series of Mashan group and its evolution. *Acta Petrologica et Mineralogica*, *11*(2), 97–108.

Jiang, Y. D., Schulmann, K., Kroener, A., Sun, M., Lexa, O., Janousek, V., et al. (2017). Neoproterozoic-early Paleozoic peri-Pacific accretionary evolution of the Mongolian collage system: Insights from geochemical and U-Pb zircon data from the Ordovician sedimentary wedge in the Mongolian Altai. *Tectonics*, *36*(11), 2305–2331. https://doi.org/10.1002/2017tc004533

Jiang, Y. D., Schulmann, K., Sun, M., Weinberg, R. F., Stipska, P., Li, P. F., et al. (2019). Structural and geochronological constraints on Devonian suprasubduction tectonic switching and Permian collisional dynamics in the Chinese Altai, Central Asia. *Tectonics*, *38*(1), 253–280. https://doi.org/10.1029/2018tc005231

Jourdan, F., Féraud, G., Bertrand, H., Watkeys, M. K., & Renne, P. R. (2007). Distinct brief major events in the Karoo large igneous province clarified by new ^{40}Ar/^{39}Ar ages on the Lesotho basalts. *Lithos*, *98*(1–4), 195–209. https://doi.org/10.1016/j.lithos.2007.03.002

Kong, L. Z., Jiang, Y. D., Schulmann, K., Zhang, J., Weinberg, R. F., Sun, M., et al. (2022). Petrostructural and geochronological constraints on Devonian extension-shortening cycle in the Chinese Altai: Implications for retreating-advancing subduction. *Tectonics*, *41*(9), e2021TC007195. https://doi.org/10.1029/2021tc007195

Koppers, A. A. (2002). ArArCALC—Software for ^{40}Ar/^{39}Ar age calculations. *Computers & Geosciences*, *28*(5), 605–619. https://doi.org/10.1016/s0098-3004(01)00095-4

Kovach, V., Salnikova, E., Wang, K. L., Jahn, B. M., Chiu, H. Y., Reznitskiy, L., et al. (2013). Zircon ages and Hf isotopic constraints on sources of clastic metasediments of the Slyudyansky high-grade complex, southeastern Siberia: Implication for continental growth and evolution of the Central Asian Orogenic Belt. *Journal of Asian Earth Sciences*, *62*, 18–36. https://doi.org/10.1016/j.jseaes.2011.08.008

Kozakov, I. K., Salnikova, E. B., Anisimova, I. V., Azimov, P. Y., Kovach, V. P., Plotkina, Y. V., et al. (2019). Tectonic position of the late neoproterozoic-early Paleozoic metamorphic belts within the Tuva-Mongolian terrane of the Central Asian Orogenic belt. *Petrology*, *27*(1), 43–58. https://doi.org/10.1134/s086959111805003x

Kozakov, I. K., Sal'nikova, E. B., Kovach, V. P., Yakovleva, S. Z., Anisimova, I. V., Kozlovsky, A. M., et al. (2015). Main stages in the evolution and geodynamic setting of the South Hangay metamorphic belt, Central Asia. *Petrology*, *23*(4), 309–330. https://doi.org/10.1134/s0869591115040049

Kozakov, I. K., Sal'nikova, E. B., Kovach, V. P., Yarmolyuk, V. V., Anisimova, I. V., Kozlovskii, A. M., et al. (2008). Vendian stage in formation of the early Caledonian superterrane in Central Asia. *Stratigraphy and Geological Correlation*, *16*(4), 360–382. https://doi.org/10.1134/s0869593808040023

Kozakov, I. K., Yarmolyuk, V. V., Kovach, V. P., Bibikova, E. V., Kirnozova, T. I., Kozlovskii, A. M., et al. (2012). The early Baikalian crystalline complex in the basement of the Dzabkhan microcontinent of the early Caledonian orogenic area, Central Asia. *Stratigraphy and Geological Correlation*, *20*(3), 231–239. https://doi.org/10.1134/s0869593812030057

Kruckenberg, S. C., Ferré, E. C., Teyssier, C., Vanderhaeghe, O., Whitney, D. L., Seaton, N. C. A., & Skord, J. A. (2010). Viscoplastic flow in migmatites deduced from fabric anisotropy: An example from the Naxos dome, Greece. *Journal of Geophysical Research*, *115*(B9), B09401. https://doi.org/10.1029/2009jb007012

Kuzmichev, A. B., & Larionov, A. N. (2013). Neoproterozoic island arcs in east Sayan: Duration of magmatism (from U-Pb zircon dating of volcanic clastics). *Russian Geology and Geophysics*, *54*(1), 34–43. https://doi.org/10.1016/j.rgg.2012.12.003

Lee, J. Y., Marti, K., Severinghaus, J. P., Kawamura, K., Yoo, H. S., Lee, J. B., & Kim, J. S. (2006). A redetermination of the isotopic abundances of atmospheric Ar. *Geochimica et Cosmochimica Acta*, *70*(17), 4507–4512. https://doi.org/10.1016/j.gca.2006.06.1563

Li, X. C., Yu, J. H., Sang, L., Luo, L., & Zhu, G. (2009). Granulite facies metamorphism of the Olkhon terrane in southern Siberian Craton and tectonic significance. *Acta Petrologica Sinica*, *25*(12), 3346–3356.

Li, Z. X., Bogdanova, S. V., Collins, A. S., Davidson, A., De Waele, B., Ernst, R. E., et al. (2008). Assembly, configuration, and break-up history of Rodinia: A synthesis. *Precambrian Research*, *160*(1–2), 179–210. https://doi.org/10.1016/j.precamres.2007.04.021

Li, Z. Y., & Jiang, Y. D. (2023). Geochronological data of Paleozoic rocks from the Olkhon terrane (southern Siberia) (version 2.0) [Dataset]. Mendeley Data. https://doi.org/10.17632/jvpbh5bygv.2

Li, Z. Y., Jiang, Y. D., Collett, S., Štípská, P., Schulmann, K., Wang, S., & Sukhorukov, V. (2023). Metamorphic and chronological constrains on the early Paleozoic tectonic-thermal evolution of the Olkhon terrane, south Siberia. *Journal of Metamorphic Geology*, *41*(4), 525–556. https://doi.org/10.1111/jmg.12706

Liu, Y. S., Hu, Z. C., Gao, S., Gunther, D., Xu, J., Gao, C. G., & Chen, H. (2008). In situ analysis of major and trace elements of anhydrous minerals by LA-ICP-MS without applying an internal standard. *Chemical Geology*, *257*(1–2), 34–43. https://doi.org/10.1016/j.chemgeo.2008.08.004

Liu, Y. S., Hu, Z. C., Zong, K. Q., Gao, C. G., Gao, S., Xu, J., & Chen, H. (2010). Reappraisement and refinement of zircon U-Pb isotope and trace element analyses by LA-ICP-MS. *Chinese Science Bulletin*, *55*(15), 1535–1546. https://doi.org/10.1007/s11434-010-3052-4

Ludwig, K. (2003). User's manual for isoplot 3.00, a geochronological toolkit for microsoft excel. *Berkeley Geochronology Center Special Publications*, *4*, 25–32.

Makrygina, V. A., Belichenko, V. G., & Reznitsky, L. Z. (2007). Types of paleoisland arcs and back-arc basins in the northeast of the Paleoasian Ocean (from geochemical data). *Russian Geology and Geophysics*, *48*(1), 107–119. https://doi.org/10.1016/j.rgg.2006.12.010

Makrygina, V. A., & Petrova, Z. I. (1998). The importance of geochemical data for geodynamic reconstruction: Formation of the Olkhon metamorphic complex, lake Baikal, Russia. *Lithos*, *43*(3), 135–150. https://doi.org/10.1016/s0024-4937(98)00010-3

Makrygina, V. A., Tolmacheva, E. V., & Lepekhina, E. N. (2014). Crystallization history of Paleozoic granitoids in the Ol'khon region, Lake Baikal (SHRIMP-II zircon dating). *Russian Geology and Geophysics*, *55*(1), 33–45. https://doi.org/10.1016/j.rgg.2013.12.010

Mekhonoshin, A. S., Vladimirov, A. G., Volkova, N. I., Kolotilina, T. B., Mikheev, E. I., Travin, A. V., et al. (2013). Restitic ultramafic rocks in the Early Caledonian collisional system of western Cisbaikalia. *Russian Geology and Geophysics*, *54*(10), 1219–1235. https://doi.org/10.1016/j.rgg.2013.09.007

Merdith, A. S., Williams, S. E., Collins, A. S., Tetley, M. G., Mulder, J. A., Blades, M. L., et al. (2021). Extending full-plate tectonic models into deep time: Linking the Neoproterozoic and the Phanerozoic. *Earth-Science Reviews*, *214*, 103477. https://doi.org/10.1016/j.earscirev.2020.103477

Mikheev, E. I., Vladimirov, A. G., Fedorovsky, V. S., Bayanova, T. B., Mazukabzov, A. M., Travin, A. V., et al. (2017). Age of overthrust-type granites in the accretionary-collisional system of the early Caledonides (western Baikal region). *Doklady Earth Sciences*, *472*(2), 152–158. https://doi.org/10.1134/s1028334x17020167

Molnar, P., & Tapponnier, P. (1977). Relation of the tectonics of eastern China to the India-Eurasia collision: Application of slip-line field theory to large-scale continental tectonics. *Geology*, *5*(4), 212–216. https://doi.org/10.1130/0091-7613(1977)5<212:rottoe>2.0.co;2

Nozhkin, A. D., Bayanova, T. B., Turkina, O. M., Travin, A. V., & Dmitrieva, N. V. (2005). *Early paleozoic granitoid magmatism and metamorphism in Derbina microcontinent of east Sayan: New isotopic-geochronological data; Rannepaleozojskij granitoidnyj magmatizm i metamorfizm v Derbinskom mikrokontinente Vostochnogo Sayana: Novye izotopno-geokhronologicheskie dannye* (p. 404). Doklady Akademii Nauk-Rossijskaya Akademiya Nauk.

Poller, U., Gladkochub, D. P., Donskaya, T. V., Mazukabzov, A. M., Sklyarov, E. V., & Todt, W. (2005). Multistage magmatic and metamorphic evolution in the Southern Siberian Craton: Archean and Palaeoproterozoic zircon ages revealed by SHRIMP and TIMS. *Precambrian Research*, *136*(3–4), 353–368. https://doi.org/10.1016/j.precamres.2004.12.003

Priyatkina, N., Ernst, R. E., & Khudoley, A. K. (2020). A preliminary reassessment of the Siberian cratonic basement with new U-Pb-Hf detrital zircon data. *Precambrian Research*, *340*, 105645. https://doi.org/10.1016/j.precamres.2020.105645

Pubellier, M., & Meresse, F. (2013). Phanerozoic growth of Asia: Geodynamic processes and evolution. *Journal of Asian Earth Sciences*, *72*, 118–128. https://doi.org/10.1016/j.jseaes.2012.06.013

Renne, P. R., Mundil, R., Balco, G., Min, K. W., & Ludwig, K. R. (2010). Joint determination of ^{40}K decay constants and ^{40}Ar*/^{40}K for the Fish Canyon sanidine standard, and improved accuracy for ^{40}Ar/^{39}Ar geochronology. *Geochimica et Cosmochimica Acta*, *74*(18), 5349–5367. https://doi.org/10.1016/j.gca.2010.06.017

Rey, P. F., Teyssier, C., & Whitney, D. L. (2009). Extension rates, crustal melting, and core complex dynamics. *Geology*, *37*(5), 391–394. https://doi.org/10.1130/g25460a.1

Richter, M., Nebel-Jacobsen, Y., Nebel, O., Zack, T., Mertz-Kraus, R., Raveggi, M., & Rösel (2019). Assessment of five monazite reference materials for U-Th/Pb dating using laser-ablation ICP-MS. *Geosciences*, *9*(9), 391. https://doi.org/10.3390/geosciences9090391

Salnikova, E., Sergeev, S., Kotov, A., Yakovleva, S., Steiger, R., Reznitskiy, L., & Vasil'ev, E. (1998). U-Pb zircon dating of granulite metamorphism in the Sludyanskiy Complex, eastern Siberia. *Gondwana Research*, *1*(2), 195–205. https://doi.org/10.1016/S1342-937X(05)70830-3

Sang, H. Q., Wang, F., He, H. Y., & Wang, Y. (2006). Intercalibration of the ZBH-15 biotite reference material utilized for K-Ar and ^{40}Ar/^{39}Ar Ar isotopic dating in China. *Bulletin of Mineralogy, Petrology and Geochemistry*, *25*(3).

Schaen, A. J., Jicha, B. R., Hodges, K. V., Vermeesch, P., Stelten, M. E., Mercer, C. M., et al. (2021). Interpreting and reporting ^{40}Ar/^{39}Ar geochronologic data. *Geological Society of America Bulletin*, *133*(3–4), 461–487. https://doi.org/10.1130/b35560.1

Schulmann, K., Lexa, O., Štípská, P., Racek, M., Tajcmanova, L., Konopasek, J., et al. (2008). Vertical extrusion and horizontal channel flow of orogenic lower crust: Key exhumation mechanisms in large hot orogens? *Journal of Metamorphic Geology*, *26*(2), 273–297. https://doi.org/10.1111/j.1525-1314.2007.00755.x

Schulmann, K., Thompson, A. B., Lexa, O., & Ježek, J. (2003). Strain distribution and fabric development modeled in active and ancient transpressive zones. *Journal of Geophysical Research*, *108*(B1), ETG6-1–ETG6-15. https://doi.org/10.1029/2001jb000632

Sengor, A. M. C., Natalin, B. A., & Burtman, V. S. (1993). Evolution of the Altaid tectonic collage and Paleozoic crustal growth in Eurasia. *Nature*, *364*(6435), 299–307. https://doi.org/10.1038/364299a0

Shu, T., Jiang, Y. D., Schulmann, K., Yu, Y., Yuan, C., Wang, S., et al. (2022). Structure, geochronology, and petrogenesis of Permian peraluminous granite dykes in the southern Chinese Altai as indicators of Altai–East Junggar convergence. *Geological Society of America Bulletin*. https://doi.org/10.1130/B36408.1

Sklyarov, E. V., & Fedorovsky, V. S. (2006). Magma mingling: Tectonic and geodynamic aspects. *Geotektonika*, *2*, 47–64.

Sklyarov, E. V., Fedorovsky, V. S., Gladkochub, D. P., & Vladimirov, A. G. (2001). Synmetamorphic mafic dikes-indicators of a collapse of collisional system of the West Baikal Area in extensional regime. *Transactions of Russian Academy of science (Doklady)*, *381*(4), 522–527.

Sklyarov, E. V., Fedorovsky, V. S., Kotov, A. B., Lavrenchuk, A. V., Mazukabzov, A. M., Levitsky, V. I., et al. (2009). Carbonatites in collisional settings and pseudo-carbonatites of the Early Paleozoic Ol'khon collisional system. *Russian Geology and Geophysics*, *50*(12), 1091–1106. https://doi.org/10.1016/j.rgg.2009.11.008

Sklyarov, E. V., Lavrenchuk, A. V., Fedorovsky, V. S., Gladkochub, D. P., Donskaya, T. V., Kotov, A. B., et al. (2020a). Regional, contact metamorphism, and autometamorphism of the Olkhon terrane (west Baikal area). *Petrology*, *28*(1), 47–61. https://doi.org/10.1134/s0869591120010051

Sklyarov, E. V., Lavrenchuk, A. V., Fedorovsky, V. S., Pushkarev, E. V., Semenova, D. V., & Starikova, A. E. (2020b). Dismembered Ophiolite of the Olkhon composite terrane (Baikal, Russia): Petrology and emplacement. *Minerals*, *10*(4), 305. https://doi.org/10.3390/min10040305

Sláma, J., Košler, J., Condon, D. J., Crowley, J. L., Gerdes, A., Hanchar, J. M., et al. (2008). Plešovice zircon — A new natural reference material for U–Pb and Hf isotopic microanalysis. *Chemical Geology*, *249*(1–2), 1–35. https://doi.org/10.1016/j.chemgeo.2007.11.005

Soejono, I., Peřestý, V., Schulmann, K., Čopjaková, R., Svojtka, M., Štípská, P., et al. (2021). Structural, metamorphic and geochronological constraints on Palaeozoic multi-stage geodynamic evolution of the Altai accretionary wedge system (Hovd Zone, western Mongolia). *Lithos*, *396–397*, 106204. https://doi.org/10.1016/j.lithos.2021.106204

Štípská, P., Schulmann, K., Lehmann, J., Corsini, M., Lexa, O., & Tomurhuu, D. (2010). Early Cambrian eclogites in SW Mongolia: Evidence that the Palaeo-Asian Ocean suture extends further east than expected. *Journal of Metamorphic Geology*, *28*(9), 915–933. https://doi.org/10.1111/j.1525-1314.2010.00899.x

Sukhbaatar, T., Lexa, O., Schulmann, K., Aguilar, C., Štípská, P., Wong, J., et al. (2022). Paleozoic geodynamics and architecture of the southern part of the Mongolian Altai zone. *Tectonics*, *41*(8), e2022TC007498. https://doi.org/10.1029/2022tc007498

Tapponnier, P., & Molnar, P. (1976). Slip-line field theory and large-scale continental tectonics. *Nature*, *264*(5584), 319–324. https://doi.org/10.1038/264319a0

Tapponnier, P., Peltzer, G., Le Dain, A., Armijo, R., & Cobbold, P. (1982). Propagating extrusion tectonics in Asia: New insights from simple experiments with plasticine. *Geology*, *10*(12), 611–616. https://doi.org/10.1130/0091-7613(1982)10<611:petian>2.0.co;2

Thompson, A. B., Schulmann, K., Jezek, J., & Tolar, V. (2001). Thermally softened continental extensional zones (arcs and rifts) as precursors to thickened orogenic belts. *Tectonophysics*, *332*(1–2), 115–141. https://doi.org/10.1016/s0040-1951(00)00252-3

Tomascak, P. B., Krogstad, E. J., & Walker, R. J. (1996). U-Pb monazite geochronology of granitic rocks from Maine: Implications for late Paleozoic tectonics in the northern appalachians. *The Journal of Geology*, *104*(2), 185–195. https://doi.org/10.1086/629813

Travin, A. V., Yudin, D. S., Vladimirov, A. G., Khromykh, S. V., Volkova, N. I., Mekhonoshin, A. S., & Kolotilina, T. B. (2009). Thermochronology of the Chernorud granulite zone, Ol'khon region, western Baikal area. *Geochemistry International*, *47*(11), 1107–1124. https://doi.org/10.1134/s0016702909110068

Turkina, O. M., Urmantseva, L. N., Berezhnaya, N. G., & Presnyakov, S. L. (2010). Paleoproterozoic age of the protoliths of metaterrigenous rocks in the east of the Irkut Granulite-Gneiss block (Sharyzhalgai salient, Siberian Craton). *Stratigraphy and Geological Correlation*, *18*(1), 16–30. https://doi.org/10.1134/s0869593810010028

Urmantseva, L. N., Turkina, O. M., & Larionov, A. N. (2012). Metasedimentary rocks of the Angara-Kan granulite-gneiss block (Yenisey Ridge, south-western margin of the Siberian Craton): Provenance characteristics, deposition and age. *Journal of Asian Earth Sciences*, *49*, 7–19. https://doi.org/10.1016/j.jseaes.2011.10.008

Vanderhaeghe, O., & Teyssier, C. (2001). Partial melting and flow of orogens. *Tectonophysics*, *342*(3–4), 451–472. https://doi.org/10.1016/s0040-1951(01)00175-5

Vanderhaeghe, O., Whitney, D., Teyssier, C., & Siddoway, C. (2004). *Structural development of the Naxos migmatite dome* (pp. 211–228). Special Publication-Geological Society of London.

Vladimirov, A. G., Khromykh, S. V., Mekhonoshin, A. S., Volkova, N. I., Travin, A. V., Yudin, D. S., & Kruk, N. N. (2008). U-Pb dating and Sm-Nd systematics of igneous rocks in the Ol'khon region (Western Baikal Coast). *Doklady Earth Sciences*, *423*(2), 1372–1375. https://doi.org/10.1134/s1028334x08090092

Vladimirov, A. G., Volkova, N. I., Mekhonoshin, A. S., Travin, A. V., Vladimirov, V. G., Khromykh, S. V., et al. (2011). The geodynamic model of formation of early Caledonides in the Olkhon region (west Pribaikalie). *Doklady Earth Sciences*, *436*(2), 203–209. https://doi.org/10.1134/s1028334x10901234

Volkova, N. I., Mikheev, E. I., Travin, A. V., Vladimirov, A. G., Mekhonoshin, A. S., & Khlestov, V. V. (2021). P-T conditions, U/Pb and ^{40}Ar/^{39}Ar isotopic ages of UHT granulites from cape Kaltygei, western Baikal region. https://doi.org/10.5800/GT-2021-12-2-0526

Volkova, N. I., Travin, A. V., Yudin, D. S., Khromykh, S. V., Mekhonoshin, A. S., & Vladimirov, A. G. (2008). The ^{40}Ar/^{39}Ar dating of metamorphic rocks of the Ol'khon region (western Baikal region). *Doklady Earth Sciences*, *420*(1), 686–689. https://doi.org/10.1134/s1028334x08040363

Volkova, N. I., Vladimirov, A. G., Travin, A. V., Mekhonoshin, A. S., Khromykh, S. V., Yudin, D. S., & Rudnev, S. N. (2010). U-Pb isotopic dating of zircons (SHRIMP-II) from granulites of the Ol'khon region of Western Baikal area. *Doklady Earth Sciences*, *432*(2), 821–824. https://doi.org/10.1134/s1028334x10060243

Wakita, K., Pubellier, M., & Windley, B. F. (2013). Tectonic processes, from rifting to collision via subduction, in SE Asia and the western Pacific: A key to understanding the architecture of the Central Asian Orogenic belt. *Lithosphere*, *5*(3), 265–276. https://doi.org/10.1130/l234.1

Wang, S. (1983). Age determinations of ^{40}Ar/^{40}K, ^{40}Ar/^{39}Ar and radiogenic ^{40}Ar released characteristics on K-Ar geostandards of China. *Chinese Journal of Geology*, *18*(4), 315–323.

Wang, S., Jiang, Y. D., Weinberg, R., Schulmann, K., Zhang, J., Li, P. F., et al. (2021). Flow of Devonian anatectic crust in the accretionary Altai Orogenic Belt, central Asia: Insights into horizontal and vertical magma transfer. *Bulletin*, *133*(11–12), 2501–2523. https://doi.org/10.1130/b35645.1

Wiedenbeck, M., Alle, P., Corfu, F., Griffin, W., Meier, M., Oberli, F. V., et al. (1995). Three natural zircon standards for U-Th-Pb, Lu-Hf, trace element and REE analyses. *Geostandards Newsletter*, *19*(1), 1–23. https://doi.org/10.1111/j.1751-908x.1995.tb00147.x

Wilde, S. A. (2015). Final amalgamation of the Central Asian Orogenic belt in NE China: Paleo-Asian Ocean closure versus paleo-Pacific plate subduction — A review of the evidence. *Tectonophysics*, *662*, 345–362. https://doi.org/10.1016/j.tecto.2015.05.006

Wilhem, C., Windley, B. F., & Stampfli, G. M. (2012). The Altaids of Central Asia: A tectonic and evolutionary innovative review. *Earth-Science Reviews*, *113*(3–4), 303–341. https://doi.org/10.1016/j.earscirev.2012.04.001

Windley, B. F., Alexeiev, D., Xiao, W. J., Kroner, A., & Badarch, G. (2007). Tectonic models for accretion of the Central Asian Orogenic belt. *Journal of the Geological Society*, *164*(1), 31–47. https://doi.org/10.1144/0016-76492006-022

Xiao, W. J., Windley, B. F., Sun, S., Li, J., Huang, B., Han, C., et al. (2015). A tale of amalgamation of three Permo-Triassic collage systems in Central Asia: Oroclines, sutures, and terminal accretion. *Annual Review of Earth and Planetary Sciences*, *43*(1), 477–507. https://doi.org/10.1146/annurev-earth-060614-105254

Xiao, W. J., Windley, B. F., Yuan, C., Sun, M., Han, C. M., Lin, S. F., et al. (2009). Paleozoic multiple subduction-accretion processes of the southern Altaids. *American Journal of Science*, *309*(3), 221–270. https://doi.org/10.2475/03.2009.02

Yudin, D. S., Khromykh, S. V., Mekhonoshin, A. S., Vladimirov, A. G., Travin, A. V., Kolotilina, T. B., et al. (2005). ^{40}Ar/^{39}Ar age and geochemical features of syncollisional gabbroids and granites from the Western Baikal Region: Evidence from the Birkhin massif and its folded framing. *Doklady Earth Sciences*, *405*(8), 1261–1265.

Zhang, W. F., Zheng, D. W., Liu, G. Q., Xu, Y. G., & Jiang, Y. D. (2021). Optimization of irradiation parameters for ^{40}Ar/^{39}Ar dating by Argus VI multi-collector mass spectrometry. *Journal of Analytical Atomic Spectrometry*, *36*(7), 1374–1380. https://doi.org/10.1039/d1ja00055a

Zhou, J. B., & Wilde, S. A. (2013). The crustal accretion history and tectonic evolution of the NE China segment of the Central Asian Orogenic Belt. *Gondwana Research*, *23*(4), 1365–1377. https://doi.org/10.1016/j.gr.2012.05.012

Zhou, J. B., Wilde, S. A., Zhang, X. Z., Ren, S. M., & Zheng, C. Q. (2011a). Early Paleozoic metamorphic rocks of the Erguna block in the Great Xing'an Range, NE China: Evidence for the timing of magmatic and metamorphic events and their tectonic implications. *Tectonophysics*, *499*(1–4), 105–117. https://doi.org/10.1016/j.tecto.2010.12.009

Zhou, J. B., Wilde, S. A., Zhang, X. Z., Zhao, G. C., Liu, F. L., Qiao, D. W., et al. (2011b). A> 1300 km late Pan-African metamorphic belt in NE China: New evidence from the Xing'an block and its tectonic implications. *Tectonophysics*, *509*(3–4), 280–292. https://doi.org/10.1016/j.tecto.2011.06.018

Zhou, J. B., Wilde, S. A., Zhao, G. C., & Han, J. (2018). Nature and assembly of microcontinental blocks within the Paleo-Asian Ocean. *Earth-Science Reviews*, *186*, 76–93. https://doi.org/10.1016/j.earscirev.2017.01.012

Zhu, M. S., Zhang, F. Q., Smit, M. A., Pastor-Galán, D., Guilmette, C., Miao, L. C., et al. (2023). Discovery of a >1,000 km Cambrian eclogite-bearing high-pressure metamorphic belt in the Central Asian Orogenic belt: Implications for the final closure of the Pan-Rodinian Ocean. *Journal of Geophysical Research: Solid Earth*, *128*(1), e2022JB025388. https://doi.org/10.1029/2022jb025388

Zonenshain, L. P., Michael, I. K., Natapov, L. M., & Benjamin, M. (1990). Geology of the USSR: A plate-tectonic synthesis, Siberian Platform (Vol. *21*).

Zorin, Y. A., Sklyarov, E., Belichenko, V., & Mazukabzov, A. (2009). Island arc–back-arc basin evolution: Implications for late Riphean–early Paleozoic geodynamic history of the Sayan–Baikal folded area. *Russian Geology and Geophysics*, *50*(3), 149–161. https://doi.org/10.1016/j.rgg.2008.06.022

Zwart, H. (1986). The Variscan geology of the Pyrenees. *Tectonophysics*, *129*(1–4), 9–27. https://doi.org/10.1016/0040-1951(86)90243-x